Icarus 292 (2017) 54–73

Contents lists available at ScienceDirect

Icarus

journal homepage: www.elsevier.com/locate/icarus

GRAIL gravity observations of the transition from complex crater to peak-ring basin on the Moon: Implications for crustal structure and impact basin formation

David M.H. Baker[a,b,*], James W. Head[a], Roger J. Phillips[c], Gregory A. Neumann[b], Carver J. Bierson[d], David E. Smith[e], Maria T. Zuber[e]

[a] Department of Geological Sciences, Brown University, Providence, RI 02912, USA
[b] NASA Goddard Space Flight Center, Greenbelt, MD 20771, USA
[c] Department of Earth and Planetary Sciences and McDonnell Center for the Space Sciences, Washington University, St. Louis, MO 63130, USA
[d] Department of Earth and Planetary Sciences, University of California, Santa Cruz, CA 95064, USA
[e] Department of Earth, Atmospheric and Planetary Sciences, MIT, Cambridge, MA 02139, USA

ARTICLE INFO

Article history:
Received 14 September 2016
Revised 1 March 2017
Accepted 21 March 2017
Available online 22 March 2017

ABSTRACT

High-resolution gravity data from the Gravity Recovery and Interior Laboratory (GRAIL) mission provide the opportunity to analyze the detailed gravity and crustal structure of impact features in the morphological transition from complex craters to peak-ring basins on the Moon. We calculate average radial profiles of free-air anomalies and Bouguer anomalies for peak-ring basins, protobasins, and the largest complex craters. Complex craters and protobasins have free-air anomalies that are positively correlated with surface topography, unlike the prominent lunar mascons (positive free-air anomalies in areas of low elevation) associated with large basins. The Bouguer gravity anomaly profiles of complex craters are highly irregular, with central positive anomalies that are generally absent or not clearly tied to interior morphology. In contrast, gravity profiles for peak-ring basins (~200 km to 580 km) are much more regular and are highly correlated with surface morphology. A central positive Bouguer anomaly is confined within the peak ring and a negative Bouguer anomaly annulus extends from the edge of the positive anomaly outward to about the rim crest. A number of degraded basins lacking interior peak rings have diameters and gravity patterns similar to those of well-preserved peak-ring basins. If these structures represent degraded peak-ring basins, the number of peak-ring basins on the Moon would increase by more than a factor of two to 34. The gravity anomalies within basins are interpreted to be due to uplift of the mantle confined within the peak ring and an annulus of thickened crust between the peak ring and rim crest. We hypothesize that mantle uplift is influenced by interaction between the transient cavity and the mantle. Further, mascon formation is generally disconnected from the number of basin rings formed and occurs over a wide range of basin sizes. These observations have important implications for models of basin and mascon formation on the Moon and other planetary bodies.

1. Introduction

After over a half-century of work, there is currently no consensus on the formation of impact basin rings on the Moon and terrestrial planets (Baldwin, 1949; Hartmann and Kuiper, 1962; Hartmann and Wood, 1971; Wood and Head, 1976; Pike and Spudis, 1987; Melosh, 1989; Spudis, 1993; Alexopoulos and McKinnon, 1994; Head, 2010; Baker et al., 2011a,b). Part of this uncertainty has been a lack of detailed understanding of the surface and subsurface characteristics of impact structures in the transition from complex craters to impact basins that may be used to refine existing models of basin formation. On most rocky planetary bodies, the onset of basin formation occurs when central peaks within complex craters are replaced by an interior ring of peaks to form peak-ring basins (Hartmann and Wood, 1971; Wood and Head, 1976; Head, 1977; Pike and Spudis, 1987; Baker et al., 2011a,b). Transitional crater forms, called protobasins, possessing both central peaks and peak rings are also observed (Pike, 1982; Pike and Spudis, 1987; Baker et al., 2011a). At the largest basin sizes, additional rings are added to form multi-ring basins (Head, 1977; Potter, 2015). Fortunately, recent data for the Moon from orbital spacecraft are helping to elucidate the characteristics of these mor-

* Corresponding author at: NASA Goddard Space Flight Center 8800 Greenbelt Rd., Code 698 Greenbelt, MD 20771, USA.
E-mail address: david.m.hollibaughbaker@nasa.gov (D.M.H. Baker).

http://dx.doi.org/10.1016/j.icarus.2017.03.024
0019-1035/

phological transitions. Image data from the Lunar Reconnaissance Orbiter Camera (LROC) and topography data from the Lunar Orbiter Laser Altimeter (LOLA) are greatly improving our understanding of the detailed surface morphometries of complex craters and peak-ring basins (Baker et al., 2011a, 2012; Baker and Head, 2013; Bray et al., 2012). Baker et al. (2011a, 2012) have shown that the change from craters to basins occurs at a diameter of ~200 km and is a discontinuous transition in depth, area, and peak characteristics. These studies also suggest that impact-melt production, retention, and mobility during the impact event (Cintala and Grieve, 1998a,b; Osinski et al., 2011) greatly affect the final surface morphometries of basins.

Our understanding of the subsurface structure of the transition from craters to basins is not as well understood. Unlike crater investigations (e.g., drilling) on Earth, we are currently incapable of directly probing the subsurface of lunar impact craters; instead, we must depend on orbital geophysical techniques. On the Moon, our understanding of global crustal structure has relied on measurements of its gravity field. Through gravity data from the Clementine, Lunar Prospector and Kaguya spacecraft, large impact basins have been shown to possess unique free-air gravity anomaly characteristics, with a central positive anomaly that is ringed by annuli of negative, then positive anomalies (Neumann et al., 1996; Namiki et al., 2009). These characteristics define the classic "mascon" (mass concentration) basin first reported by Muller and Sjogren (1968) from Lunar Orbiter tracking data. Previous interpretations of mascon subsurface structure suggested that the mantle is uplifted in a super-isostatic state in the centers of the basins (Neumann et al., 1996). Bouguer gravity data derived from an improved understanding of surface topography also suggested the presence of annuli of thickened crust surrounding these super-isostatic "mantle plugs" (Neumann et al., 1996; Wieczorek and Phillips, 1999). More recent models of mascon formation (Andrews-Hanna, 2013; Melosh et al., 2013; Freed et al., 2014) suggest that the super-isostatic state of these mantle uplifts is a result of post-impact crustal adjustments. While it has been possible to infer the crustal structure beneath large basins (>300 km in diameter) from previous gravity measurements, the resolution of those datasets, especially for the lunar farside, inhibited analysis of the crater-to-basin transition and detailed linkages to surface morphology at smaller diameters.

Recent high-resolution measurements of the lunar gravity field by the twin Gravity Recovery and Interior Laboratory (GRAIL) spacecraft (Zuber et al., 2013a,b) now provide the opportunity to analyze the gravity and crustal structure of complex craters and peak-ring basins in great detail. Neumann et al. (2015) has compiled an updated list of lunar impact basins greater than about 200 km in diameter and recognized on the basis of topography and GRAIL gravity data, observing several characteristics of that population. Most basins larger than about 200 km were found to possess a central positive Bouguer anomaly (BA) within the innermost peak ring, with a negative BA extending outward from the peak ring to the rim crest. A well-defined trend of increasing central BA with increasing rim-crest diameter was found for basins larger than 200 km. These observations suggest that substantial mantle uplifts and crater excavation occur mainly within the peak ring, which both become greater in magnitude with increasing basin size. Further, the identified Bouguer-anomaly patterns were found to be fundamental characteristics of all impact basins; they were used to identify topographically degraded basins and to provide a more complete catalog of large impact structures on the Moon. High-resolution gravity and numerical analyses of the Orientale multi-ring basin have also been recently completed (Johnson et al., 2016; Zuber et al., 2016), which place constraints on the locations, characteristics, and formation of basin rings and excavation cavities.

Here, we complement the work of Neumann et al. (2015) by providing a more detailed assessment of the structural changes that occur in the transition from craters to basins on the Moon. In particular, detailed measurements of surface morphology are compared with data from GRAIL on both free-air and Bouguer anomalies to determine the linkage between surface and subsurface structure. These observations provide important constraints for models of mascon and peak-ring and multi-ring basin formation on the Moon and other terrestrial bodies.

2. Methods

2.1. Data

We used a degree 660, spherical-harmonic, free-air gravity model for the Moon (GRAIL JGGRAIL_660C6A), which was produced by the Jet Propulsion Laboratory (JPL) with the software tool MIRAGE (Multiple Interferometric Ranging and GPS Ensemble) (Zuber et al., 2013b). This model incorporates GRAIL observations from both the primary and the extended missions up to November 13, 2012. By comparison, Neumann et al. (2015) used a degree 900 gravity model (GRGM900C) produced by the NASA Goddard Space Flight Center (GSFC) that also includes GRAIL observations from the primary and full extended missions (Lemoine et al., 2014). While the JPL and GSFC models differ in use of software, *a priori* models, data editing, and parameter estimation, their results are largely comparable, especially at the scales of the features analyzed herein (Konopliv et al., 2013; Lemoine et al., 2014). Topographic data are from the Lunar Orbiter Laser Altimeter (LOLA) and are represented by spherical-harmonic coefficients (http://www.ipgp.fr/~wieczor/SH/SH.html). Bouguer gravity maps were generated from spherical-harmonic coefficients obtained by subtracting finite-amplitude Bouguer corrections (Wieczorek and Phillips, 1998) from JGGRAIL_660C6A, assuming a uniform crustal density of 2560 kg m^{-3}.

Models of crustal thickness and relief of the crust-mantle boundary on the Moon (herein called the "Moho") have been generated by Wieczorek et al. (2013). In them, the observed gravity from GRAIL was assumed to result from relief along the surface, relief along the crust-mantle interface, and lateral variations in density of the crust. LOLA data were used for surface relief. Following Wieczorek and Phillips (1998), Wieczorek et al. (2013) solved for the spherical-harmonic coefficients of the first-order term of the crust-mantle boundary relief, multiplied by the spatially varying density contrasts between the crust and mantle. The grain density (density in absence of porosity) of the crust was estimated using 5° gridded Lunar Prospector estimates of elemental abundances, discarding pixels that contain mare, combined with an empirical correlation between grain density and composition (Wieczorek et al., 2013). Bulk density (grain density with porosity) was obtained by multiplying the grain-density map by $1-\phi$, where ϕ is the porosity, which was assumed to be 7% or 12% in models by Wieczorek et al. (2013). To obtain a unique crustal-thickness model, they then varied the average thickness of the crust and the mantle density to find a solution that fit the seismic constraints at the Apollo 12 and 14 sites along with a minimum crustal thickness constraint of <1 km. Four models were given, representing the range of values constrained by observations, including 30 km or 38 km Apollo seismic constraints on crustal thickness and constraints of 7% to 12% crustal porosity. Here, we use their Model 1, which assumes a 29.9-km thick crust under the Apollo landing sites and 12% crustal porosity. This model produces the thinnest globally averaged crust at 34 km. Model 2 of Wieczorek et al. (2013) produces an average crustal thickness of 35 km by assuming a 30.8 km Apollo seismic constraint and 7% porosity. A globally averaged thickness of 43 km is obtained using Models 3 and 4, which use an Apollo seismic

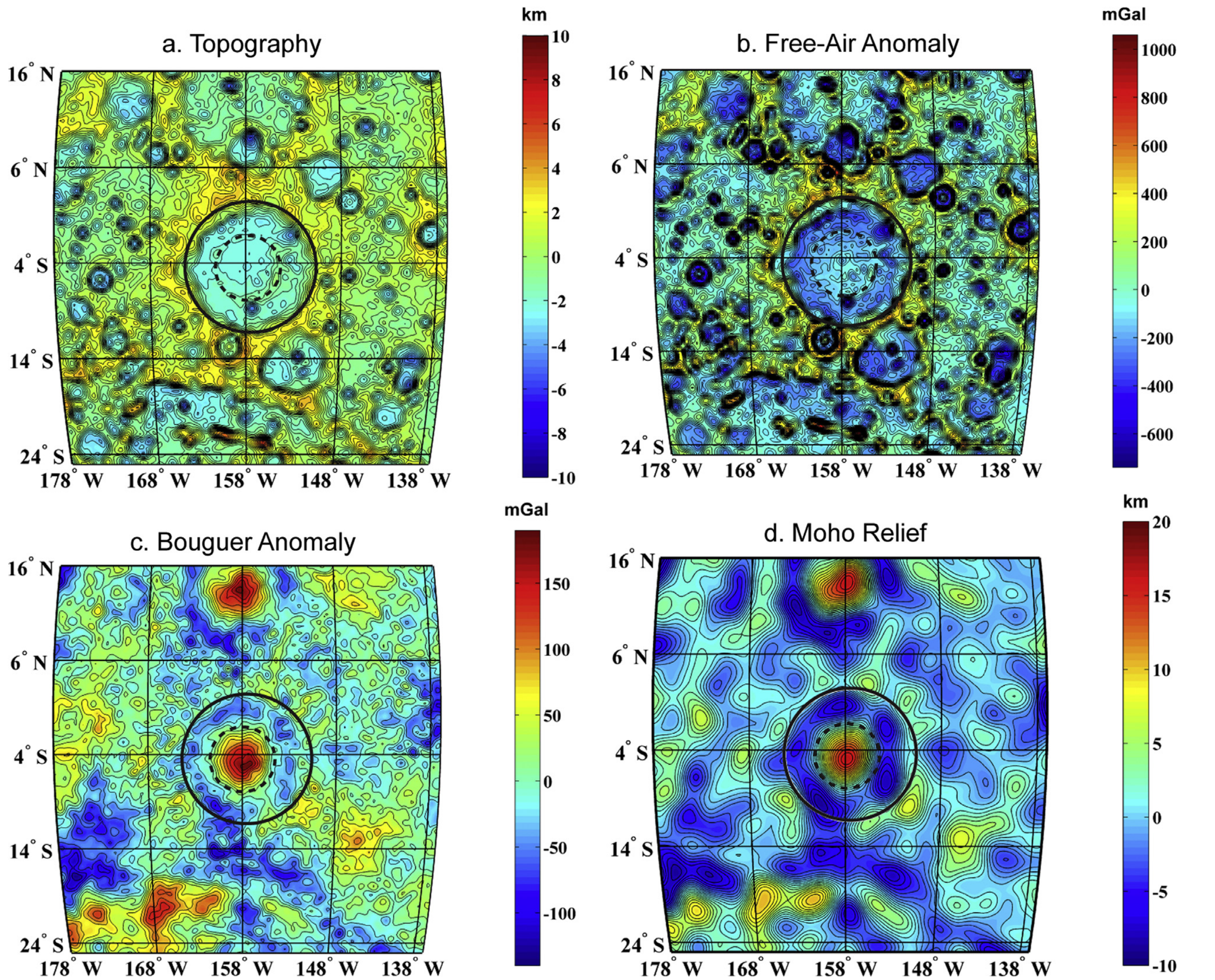

Fig. 1. Representative topography and gravity maps of Korolev basin (417 km diameter; 4.44°S, 157.47°W). (a) LOLA topography, 1-km contour interval. (b) Free-air gravity anomaly, 100-mGal contour interval. (c) Bouguer gravity anomaly, 20-mGal contour interval. (d) Moho relief, 1-km contour interval. All maps are 16- to 310-degree spherical-harmonic expansions. The solid circular outline indicates the rim crest of the basin and the dashed circle is the outline of the peak ring.

constraint of ~38 km and crustal porosities of 7% or 12%, respectively.

In order to reduce the effects of regional (long-wavelength) patterns on our analyses, we high-pass filtered the various spherical harmonic fields by removing degrees (l) lower than 16, which corresponds to a block size larger than about 330 km. We did not expand the fields beyond $l = 310$ so we could use Moho relief results from Wieczorek et al. (2013). Grids for each crater and basin were generated from the spherical-harmonic expansions at 1/4° spacing and out to three basin radii from the crater or basin center (Fig. 1).

2.2. Crater and basin measurements

Catalogs from Baker et al. (2011a) were used to determine the locations of all protobasins ($N = 3$, where N is the total number) and peak-ring basins ($N = 17$) on the Moon. We also examined a subset of complex craters > 100 km in diameter ($N = 74$), from the catalog of craters with central peaks by Baker and Head (2013). Centroids of visual circle-fits to the rim-crests using LOLA topography (Head et al., 2010; Baker et al., 2011a; Baker and Head, 2013) provide the center locations and rim-crest diameters and radii of the structures (Table 1). To analyze the general gravity characteristics of the craters and basins, we measured zonally averaged profiles starting at the center of each structure out to three crater radii (Fig. 2). Points along each profile (Fig. 2b) represent mean grid values falling within concentric rings with 5-km widths. Uncertainties in the profile are shown as one standard deviation for the samples in a ring. Averaging in this fashion assumes that the basins are symmetrical in their gravity and topographic signatures. This is a reasonable approximation for most basins, but slight offsets in central anomalies from our central values do occur (Fig. 2a), and irregular variations are more prominent in complex craters. Despite these offsets and asymmetrical variations, we feel that the assumption of symmetry is valid for our purposes, which is to capture the general gravity signatures with distance from the center for impact structures within the complex crater to peak-ring basin transition. To simplify the display of profiles, we plot average values as a single solid line (linear interpolation of mean values), with uncertainties as shaded regions (Fig. 2b).

From these average profiles, we can begin to tie the gravity signatures and associated models with surface morphometries, namely the interior peaks and rim crests, as measured by prior workers (Hale and Head, 1979; Baker et al., 2011a). In Sections 3 and 4 we seek to do this by measuring the locations of four major gravity-anomaly features in averaged radial profiles (Fig. 2) for peak-ring basins, protobasins, and complex craters. These major

Table 1
Listing of properties of analyzed peak-ring basins, protobasins, complex craters, and candidate peak-ring basins.

Name	ID	Latitude	Longitude	D_r	D_{pk}	R	R_{pk}	Mare[e]	Age[f]
Peak-ring basins[a]									
Schwarzschild	1	70.36	120.09	207	71	103.5	35.5	n	Nectarian
d'Alembert	2	51.05	164.84	232	106	116	53	n	Nectarian
Milne	3	−31.25	112.77	264	114	132	57	n	pre-Nectarian
Bailly	4	−67.18	−68.80	299	130	149.5	65	n	Nectarian
Poincare	5	−57.32	163.15	312	175	156	87.5	y	pre-Nectarian
Coulomb-Sarton[h]	6	51.35	−122.53	Not Analyzed; multi-ring basin					pre-Nectarian
Planck	7	−57.39	135.09	321	160	160.5	80	p	pre-Nectarian
Schrödinger	8	−74.90	133.53	326	150	163	75	y, FF	Lower Imbrian
Mendeleev	9	5.44	141.14	331	144	165.5	72	n	Nectarian
Birkhoff	10	58.88	−146.58	334	163	167	81.5	n	pre-Nectarian
Lorentz	11	34.30	−97.00	351	173	175.5	86.5	y	pre-Nectarian
Schiller-Zucchius[h]	12	−55.72	−45.18	361	179	180.5	89.5	y	pre-Nectarian
Korolev	13	−4.44	−157.47	417	206	208.5	103	n	Nectarian
Moscoviense	14	26.34	147.36	Not Analyzed; double impact					Nectarian
Grimaldi	15	−5.01	−68.69	460	234	230	117	y	pre-Nectarian
Apollo	16	−36.09	−151.48	492	247	246	123.5	y	pre-Nectarian
Freundlich-Sharonov[h]	17	18.35	175.00	582	318	291	159	p	pre-Nectarian
Protobasins[b]									
Antoniadi	1	−69.35	−172.96	137	56	68.5	28	y	Upper Imbrian
Compton	2	55.92	103.96	166	73	83	36.5	y, FF	Lower Imbrian
Hausen	3	−65.34	−88.76	170	55	85	27.5	n	Eratosthenian
Complex Craters[c]									
Levi-Civita	1	−23.25	143.20	100	23	50	11.5	n	pre-Nectarian
Buffon	2	−40.59	−133.54	100	23	50	11.5	p	Nectarian
Fitzgerald	3	26.85	−172.21	100	23	50	11.5	n	Nectarian
Isaev	4	−17.62	147.42	102	24	51	12	y	pre-Nectarian
Blancanus	5	−63.76	−22.00	103	24	51.5	12	p	Nectarian
Piazzi	6	−36.28	−68.20	103	24	51.5	12	y	pre-Nectarian
Mees Y	7	16.00	−97.02	103	24	51.5	12	y	pre-Nectarian
Schuster	8	4.46	146.43	103	24	51.5	12	n	Nectarian
Pascal	9	74.40	−70.10	103	24	51.5	12	p	Nectarian
Langemak	10	−9.85	119.58	104	24	52	12	y	Upper Imbrian
Saha	11	−1.75	102.91	107	25	53.5	12.5	n	Nectarian
Rumford T	12	−28.60	−172.10	108	25	54	12.5	p	pre-Nectarian
Fizeau	13	−58.21	−133.95	108	25	54	12.5	n	Upper Imbrian
Plaskett	14	81.66	176.50	109	26	54.5	13	n	Upper Imbrian
van der Waals	15	−43.56	120.04	110	26	55	13	p	pre-Nectarian
Volta	16	54.03	−84.65	110	26	55	13	y, FF	pre-Nectarian
Numerov	17	−70.55	−162.62	111	26	55.5	13	n	Nectarian
Seyfert	18	29.35	114.53	111	26	55.5	13	n	Nectarian
Gassendi	19	−17.49	−40.01	112	26	56	13	y, FF	Nectarian
Stefan	20	46.30	−108.80	112	26	56	13	p	pre-Nectarian
Ostwald	21	10.26	121.96	112	26	56	13	n	pre-Nectarian
Maurolycus	22	−41.85	13.94	113	27	56.5	13.5	p	Nectarian
Hevelius	23	2.24	−67.38	113	27	56.5	13.5	y, FF	Nectarian
Wiener	24	41.02	146.63	114	27	57	13.5	n	Nectarian
Alphonsus	25	−13.41	−2.84	114	27	57	13.5	y, FF	Nectarian
Kovalevskaya	26	30.87	−129.40	115	27	57.5	13.5	p	Upper Imbrian
Moretus	27	−70.66	−5.44	116	27	58	13.5	n	Eratosthenian
Leeuwenhoek	28	−29.28	−178.78	117	28	58.5	14	y	Nectarian
Kurchatov	29	38.40	141.78	117	28	58.5	14	n	Nectarian
Demonax	30	−78.45	59.30	120	29	60	14.5	n	Nectarian
Nernst	31	35.52	−94.67	123	29	61.5	14.5	y, FF	Nectarian
Michelson	32	6.63	−121.61	123	29	61.5	14.5	n	Nectarian
Stebbins	33	64.13	−142.63	123	29	61.5	14.5	p	pre-Nectarian
Rontgen	34	33.06	−91.53	123	29	61.5	14.5	y	NO AGES IN CATALOG
Sklodowska	35	−18.04	96.12	126	30	63	15	n	NO AGES IN CATALOG
Carnot	36	52.04	−144.02	126	30	63	15	p	Nectarian
Chaplygin	37	−5.68	150.36	128	31	64	15.5	p	Nectarian
Poynting	38	17.63	−133.38	128	31	64	15.5	p	Nectarian
Walther	39	−33.25	0.57	128	31	64	15.5	p	pre-Nectarian
Pythagoras	40	63.62	−62.83	129	31	64.5	15.5	n	Eratosthenian
Fleming	41	14.94	109.47	129	31	64.5	15.5	p	Nectarian
Aitken	42	−16.36	173.03	130	31	65	15.5	y	Upper Imbrian
Langrenus	43	−8.78	61.06	131	31	65.5	15.5	n	Eratosthenian
Albategnius	44	−11.22	3.93	133	32	66.5	16	p	Nectarian
Blackett	45	−37.41	−115.89	134	32	67	16	n	pre-Nectarian
Cleomedes	46	27.61	55.48	136	33	68	16.5	y, FF	Nectarian
Sommerfeld	47	64.58	−161.07	139	33	69.5	16.5	n	Nectarian
Mendel	48	−48.83	−109.90	142	34	71	17	y	Nectarian
Longomontanus	49	−49.86	−22.05	144	35	72	17.5	p	Nectarian
van de Graaff	50	−28.19	170.65	146	35	73	17.5	y	Nectarian
Neper	51	8.85	84.72	148	36	74	18	y	Nectarian

(*continued on next page*)

Table 1 (*continued*)

Name	ID	Latitude	Longitude	D_r	D_{pk}	R	R_{pk}	Mare[e]	Age[f]
Maginus	52	−50.21	−6.22	148	36	74	18	p	pre-Nectarian
Curie	53	−23.00	92.49	148	36	74	18	n	pre-Nectarian
Roche	54	−42.21	136.51	153	37	76.5	18.5	y	Nectarian
unnamed[i]	55	−13.54	123.94	154	37	77	18.5	n	NO AGES IN CATALOG
Hedin	56	2.60	−76.64	158	38	79	19	y	pre-Nectarian
Keeler	57	−9.70	161.96	161	39	80.5	19.5	n	Lower Imbrian
Riccioli	58	−2.80	−74.51	161	39	80.5	19.5	y	pre-Nectarian
Drygalski	59	−79.88	−87.88	165	40	82.5	20	p	pre-Nectarian
Heaviside	60	−10.34	166.84	168	41	84	20.5	p	pre-Nectarian
Rozhdestvenskiy	61	85.17	−159.50	169	41	84.5	20.5	n	pre-Nectarian
Joliot	62	25.86	93.44	169	41	84.5	20.5	y	pre-Nectarian
Gauss	63	35.94	79.11	169	41	84.5	20.5	y, FF	Nectarian
Von Karman	64	−44.63	176.01	172	42	86	21	y	pre-Nectarian
Hilbert	65	−18.06	108.25	173	42	86.5	21	n	Nectarian
Chebyshev	66	−34.00	−133.01	175	43	87.5	21.5	n	Nectarian
Fabry	67	43.05	100.82	177	43	88.5	21.5	p	pre-Nectarian
Petavius	68	−25.39	60.84	180	44	90	22	y, FF	Lower Imbrian
Mach	69	18.21	−149.27	180	44	90	22	p	pre-Nectarian
Tsiolkovskiy	70	−20.26	128.98	185	45	92.5	22.5	y	Upper Imbrian
Zeeman	71	−75.04	−135.60	185	45	92.5	22.5	p	Nectarian
Bel'kovich	72	61.57	90.20	204	50	102	25	y, FF	Nectarian
Humboldt	73	−27.12	81.06	205	51	102.5	25.5	y, FF	Upper Imbrian
Candidate Peak-ring Basins[d]									
Oppenheimer	1	−35.44	−166.04	206	88	103	44	y	Nectarian
Schickard[g]	2	−44.53	−54.98	223	97	111.5	48.5	y	pre-Nectarian
Poczobutt	3	57.68	−99.59	225	98	112.5	49	p	pre-Nectarian
Pasteur[g]	4	−11.46	104.81	231	101	115.5	50.5	n	pre-Nectarian
Landau[g]	5	42.22	−119.17	236	104	118	52	p	pre-Nectarian
Campbell[g]	6	45.50	152.96	237	105	118.5	52.5	y	pre-Nectarian
Deslandres	7	−32.81	−5.33	240	106	120	53	y	pre-Nectarian
Leibnitz	8	−38.19	179.23	247	110	123.5	55	y	pre-Nectarian
Iridum	9	44.84	−31.67	252	113	126	56.5	y	Lower Imbrian
von Karman M	10	−47.08	176.24	255	114	127.5	57	y	pre-Nectarian
Fermi	11	−19.77	123.45	259	116	129.5	58	n	pre-Nectarian
Gagarin	12	−19.61	149.24	265	120	132.5	60	n	pre-Nectarian
Harkhebi	13	40.03	98.62	280	128	140	64	n	pre-Nectarian
Sikorsky-Rittenhouse[h]	14	−68.59	109.71	282	129	141	64.5	n	Nectarian
Balmer-Kapteyn[g,h]	15	−15.76	69.64	300	139	150	69.5	p	pre-Nectarian
Ingenii[h]	16	−32.86	163.76	342	163	171	81.5	y	pre-Nectarian
Amundsen-Ganswindt[g,h]	17	−80.59	124.36	377	183	188.5	91.5	n	pre-Nectarian
Dirichlet-Jackson[h]	18	13.39	−158.24	452	228	226	114	n	NO AGES IN CATALOG

[a] Peak-ring basin rim-crest diameters (D_r), peak-ring diameters (D_{pk}), corresponding radii (R and R_{pk}) and center latitudes and longitudes from Baker et al. (2011a). All longitudes are positive eastward and negative westward.

[b] Protobasin rim-crest diameters (D_r), peak-ring diameters (D_{pk}), corresponding radii (R and R_{pk}) and center latitudes and longitudes from Baker et al. (2011a).

[c] Complex crater rim-crest diameters (D_r), corresponding radii (R) and center latitudes and longitudes from Head et al. (2010). Central peak diameters (D_{pk}) and corresponding radii (R_{pk}) are from the relationship of Hale and Head (1979), $D_{pk} = 0.259D_r - 2.57$. These are craters larger than 100 km in diameter and with central peaks from the catalog of Baker and Head (2013).

[d] Candidate peak-ring basin rim-crest diameters (D_r), corresponding radii (R) and center latitudes and longitudes measured in this study. Peak-ring diameters (D_{pk}) and corresponding radii (R_{pk}) are from the relationship of Baker et al. (2011a), $D_{pk} = 0.14{D_r}^{1.21}$.

[e] Presence or absence of mare deposits in the crater or basin interior: y = yes, n = no, p = possible (possible cryptomare, smooth fill of moderate albedo, etc.). Those craters and basins with floor fractures are denoted by "FF."

[f] Crater age designation, as compiled by the Lunar Planetary Institute (LPI) Lunar Impact Crater Database, http://www.lpi.usra.edu/lunar/surface/Lunar_Impact_Crater_Database_v24May2011.xls (Losiak et al., 2009). Most ages in that catalog are from Wilhelms (1987).

[g] Ringed basins proposed by Pike and Spudis (1987). A re-analysis of these basins by Baker et al. (2011a) and this study shows that these basins do not preserve interior peaks.

[h] Name not IAU approved, but appears in previous basin catalogs (e.g., Wilhelms, 1987).

[i] Provisional names provided here for unnamed craters.

profile features include the central maximum ("1" in Fig. 2b), first zero crossing ("2" in Fig. 2b), interior minimum ("3" in Fig. 2b), and second zero crossing ("4" in Fig. 2b). The central maximum is defined by the maximum value within 0.5R (where R is the crater or basin radius); it has an associated uncertainty of one standard deviation. The location of the central maximum is determined by finding the smallest ring whose outer radius R_o surrounds all of the central anomaly. The radius of the central anomaly is then taken to equal $R_o - 0.5(R_o - R_i)$, where R_i is the inner diameter of the 5-km-wide ring; the radius of the central anomaly then reduces to R_0 − 2.5 km. The uncertainty in this location is thus given as ±2.5 km. For BAs in peak-ring basins, the central-maximum value always occurs near the basin center (Fig. 2b). The interior minimum is defined as the minimum value within 1R. The uncertainties and location of the interior minimum are reported similarly to the central maximum. In BA profiles of peak-ring basins, the interior minimum is typically located at about 0.75R, representing a trough in a broad negative anomaly annulus (Fig. 2b). The first zero crossing is defined as the location where the average profile first crosses the anomaly axis at a value of zero moving outward from the center. To determine this location, we applied a linear interpolation between our ring-averaged data points. If the profile has a positive central anomaly, as is the case for BAs of peak-ring basins, the first zero crossing defines the radius of this central positive anomaly (Fig. 2b). For profiles without a positive central anomaly, the first zero crossing is much more variable. The second zero crossing is defined as the next location where the linearly interpolated, average profile crosses zero. This location represents the outer

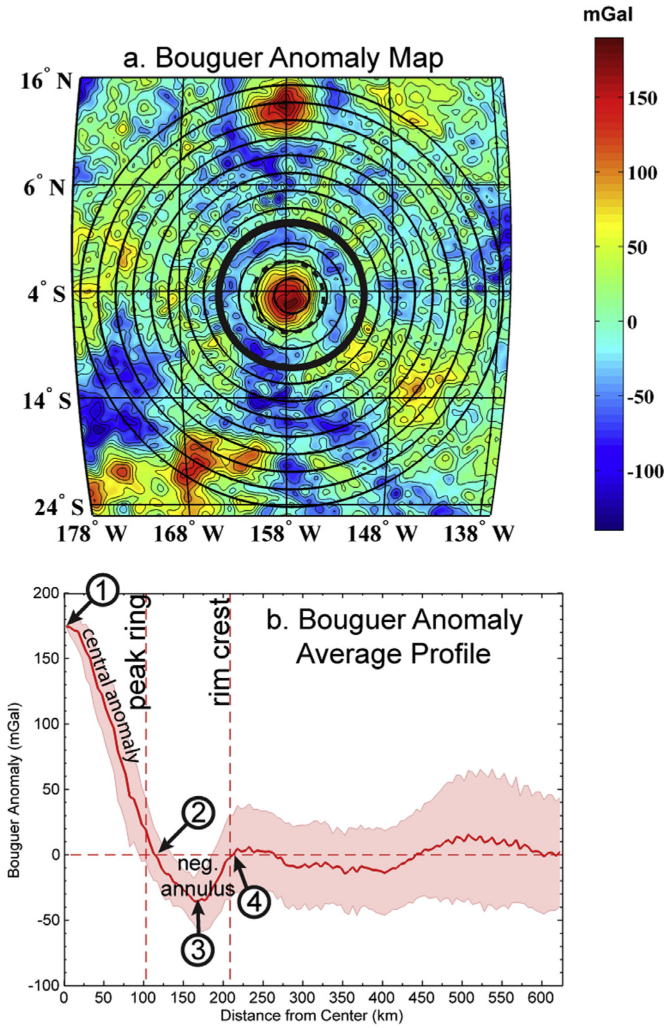

Fig. 2. Method of calculating average radial profiles of gravity, topography, and models of crustal structures for craters and basins. (a) For demonstration, a map of Bouguer gravity anomalies for Korolev (417 km diameter; 4.44°S, 157.47°W). Averages of all grid values located within concentric rings 5 km in width were calculated to determine a radial profile for each crater and basin (b). Uncertainties from the averaging are shown as one standard deviation (shaded regions in b). For clarity, only rings spaced at 50 km are shown in (a). Profiles were used to identify the locations and values of main features. For Bouguer anomalies, these are: (1) Central maximum, (2) First zero crossing (representing the diameter of the central positive anomaly, if present), (3) Interior minimum, and (4) Second zero crossing (representing the maximum radial extent of the negative annulus).

diameter of the negative annulus in BA profiles of peak-ring basins (Fig. 2b). It often does not exist in the topographic profiles of complex craters considered here (i.e., profiles have only one zero crossing or are completely negative or positive).

We also apply the above techniques to profiles of Moho relief and crustal thickness (Wieczorek et al., 2013). Moho relief is measured relative to a mean depth of 34 km in Model 1 of Wieczorek et al. (2013). Variations in Moho relief about the mean (or zero) mimic the shape of the BAs, as most of the density variations reflected in the BA are due to mantle topography with relatively minor contributions from lateral density variations in the crust (Wieczorek et al., 2013). All crustal-thickness variations are measured relative to the mean crustal thickness at $3R$ (t), which varies from basin to basin depending on its geographic location. Instead of a central maximum and annular minimum, we measure a central minimum and annular maximum in crustal thickness, as this parameter is inversely related to the magnitude of the mantle uplift (Section 4).

After initial examination of the profiles of peak-ring basins, we identified anomalous patterns for Coulomb-Sarton and Moscoviense. As noted by Neumann et al. (2015) and discussed in Section 5, we suggest that, based on its Bouguer gravity profile, Coulomb-Sarton is more analogous to a multi-ring basin. Moscoviense has recently been attributed to a double impact (Ishihara et al., 2011), where the three-ring pattern of Moscoviense is actually a peak-ring basin superposed on a larger, more degraded basin, rather than an oblique impact as early workers have proposed (see discussion in Thaisen et al., 2011). Regardless of its mode of formation, the gravity signal of Moscoviense is highly asymmetrical, and the strength of its Bouguer gravity anomaly is much greater than that predicted for a peak-ring basin of its size. As a result of their unique gravity signatures, we have chosen to remove these two basins from the presentation of results herein. However, calculated parameters for Coulomb-Sarton and Moscoviense are included in the accompanying supplementary material.

2.3. Effects of mare on the gravity profiles

We have not sought to remove the gravitational effects of interior mare fill here. Table 1 lists the craters and basins examined, indicating those with mare deposits in their interiors. We find that 6 out of 15 (6/15) peak-ring basins, 2/3 protobasins, 26/73 complex craters and 8/18 candidate peak-ring basins analyzed here have mare deposits within them. However, the thickness and spatial extents of these deposits vary considerably from very isolated patches to those that completely cover the floors of the craters or basins. In no case, though, was mare material thick enough to completely cover or obscure central peaks or peak rings. Further, we found that removing those craters and basins with mare fill and correcting for estimates of the gravity contribution of mare within peak-ring basin (see Appendix A) did not change the overall trends presented here. More detailed modeling of the contributions of mare infill is needed; however this is complicated by uncertainties in the geometries of the deposits, which may be highly irregular depending on the topography of underlying basement rocks.

3. Gravity characteristics

3.1. Free-air anomalies

Large basins on the Moon, including those with multiple rings, are generally associated with positive free-air gravity anomalies that are interpreted to be largely related to super-isostatic uplift of the mantle (Neumann et al., 1996; Wieczorek and Phillips, 1999; Melosh et al., 2013; Zuber et al., 2013b; Neumann et al., 2015). All but six (Schwarzschild, d'Alembert, Bailly, Mendeleev, Birkhoff, and Korolev) of the 15 peak-ring basins analyzed show central positive free-air anomalies in their averaged profiles that are not associated with elevated central topography (Fig. 3). These central anomalies are confined within the peak ring and the central maximum shows an apparent increase with basin diameter (Fig. 3). Six of the nine basins that have central positive free-air anomalies also have been infilled with mare lavas to varying degrees, which could be contributing to their gravity characteristics. However, positive central anomalies are observed in basins without mare infill (e.g., Milne and Freundlich-Sharonov), and positive free-air anomalies do not appear over some areas of mare that are within the basins but exterior to the peak rings, suggesting that the mare contributions to the gravity field may be relatively minor. Since the free-air anomalies for all of the peak-ring basins are generally correlated with surface topography, the mean free-air anomalies within one rim-crest radius are negative (Fig. 4a). The free-air anomalies in protobasins and complex craters are also highly correlated with to-

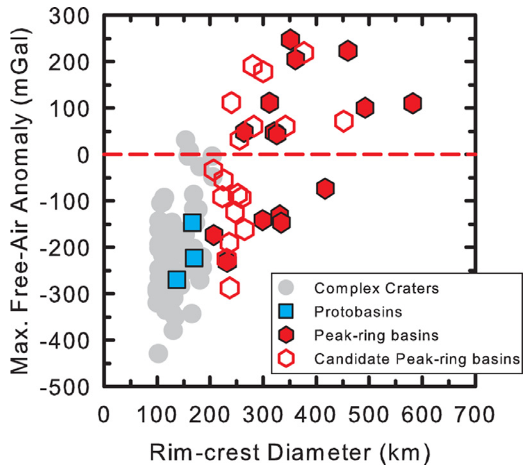

Fig. 3. Maximum free-air gravity anomaly within 0.5R as a function of rim-crest diameter for complex craters (gray circles), protobasins (blue squares), peak-ring basins (solid red hexagons), and candidate peak-ring basins (open red hexagons). (For interpretation of the references to colour in this figure legend, the reader is referred to the web version of this article.)

pography, showing negative average free-air anomalies within 1R (Fig. 4b and c). In general, no central positive free-anomalies are observed in protobasins or complex craters (Figs. 3 and 4b and c).

3.2. Bouguer anomalies (BAs)

Peak-ring basins show very regular BA patterns that are well-correlated with their unique surface morphologies (Fig. 5a). As observed earlier for larger impact basins (Neumann et al., 1996; Namiki et al., 2009) and more recently for all known lunar peak-ring basins and multi-ring basins (Neumann et al., 2015), every peak-ring basin is marked by a central positive BA, which is surrounded by a negative-Bouguer annulus that is smaller in magnitude (Figs. 5a and 6a,b). The maximum value of the BA for each peak-ring basin occurs at or near the center of the basin. As shown in Fig. 6a, the central maximum increases linearly with increasing rim-crest diameter for peak-ring basins, from values of 30 mGal to 420 mGal. The radius of each peak-ring basin's central anomaly is correlated remarkably well with the location of its peak ring (Fig. 5a). That is, the central positive BA is almost invariably located completely within the peak ring, an observation that was not possible prior to the high-resolution gravity field provided by GRAIL. We calculate a mean peak-ring radius of $0.48R \pm 0.05R$ (Baker et al., 2011a), and a mean radius of the central positive BA (i.e., the first zero crossing) of $0.47R \pm 0.1R$. Similar trends in the magnitudes and diameters of the central positive BAs were observed by Neumann et al. (2015). Absolute values reported here have slight differences when compared with those of Neumann et al. (2015) due to differences in methods of calculating the Bouguer anomalies. Despite these differences, the overall trends are in good agreement.

The negative-anomaly annulus extends from the edge of the central positive anomaly and reaches a minimum at approximately midway between the peak ring and rim crest, or at a mean value of $0.74R \pm 0.06R$ (Fig. 5a). The magnitude of this interior minimum also appears to trend linearly with rim-crest diameter (Fig. 6b), with the largest magnitudes occurring in the largest peak-ring basins. The ratio of the magnitude of the interior minimum BA to the central maximum BA is fairly constant at a mean value of 0.23 ± 0.1, excluding the anomalous value of d'Alembert at 1.47. Interestingly, the interior minima for peak-ring basins also appear to be slightly farther inward from the rim crest at the largest sizes (Fig. 5a), as the location of the interior minimum ranges from around 0.8R at the smallest basins to around 0.7R at the largest sizes. The outer edge of the negative annulus is more variable, but is generally confined to be within 1.5R and often near the rim crest of the basin.

Protobasins and complex craters, on the other hand, show very irregular BA profiles that are not obviously correlated with surface morphological features (Fig. 5a and b). Only 7 of the largest 25 complex craters have positive BAs confined to their interiors (Fig. 5b) and none of the protobasins shows a positive central Bouguer anomaly (Fig. 5a). The location of the central maximum

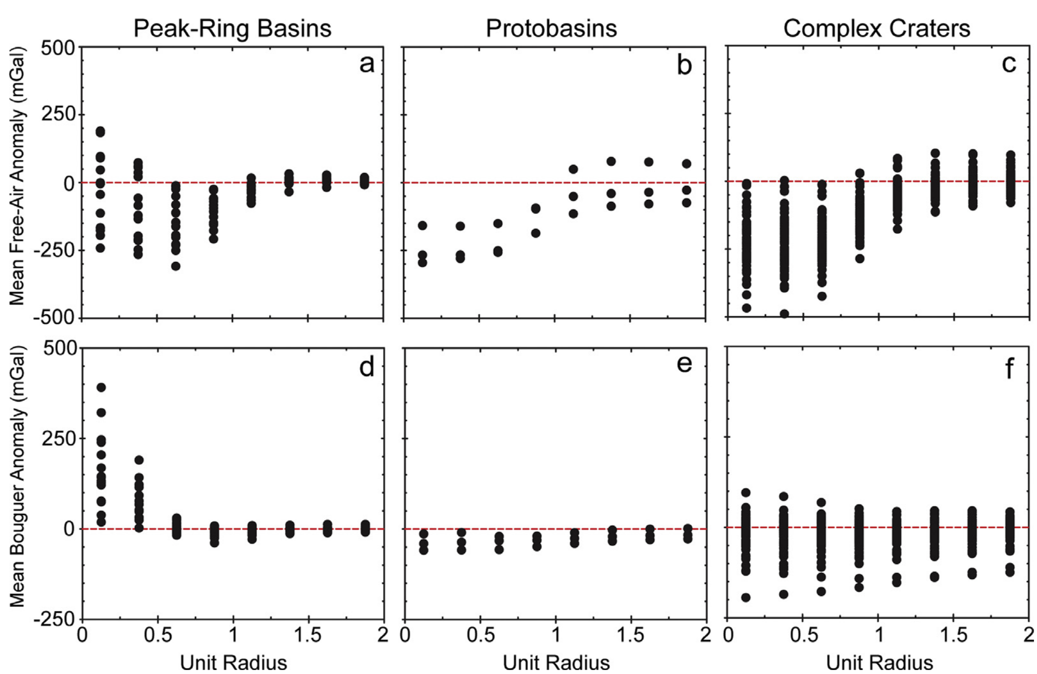

Fig. 4. Mean values of free-air (a-c) and Bouguer (d-f) gravity anomalies calculated within circles incremented by 0.25 unit radii for all peak-ring basins, protobasins, and complex craters (Table 1).

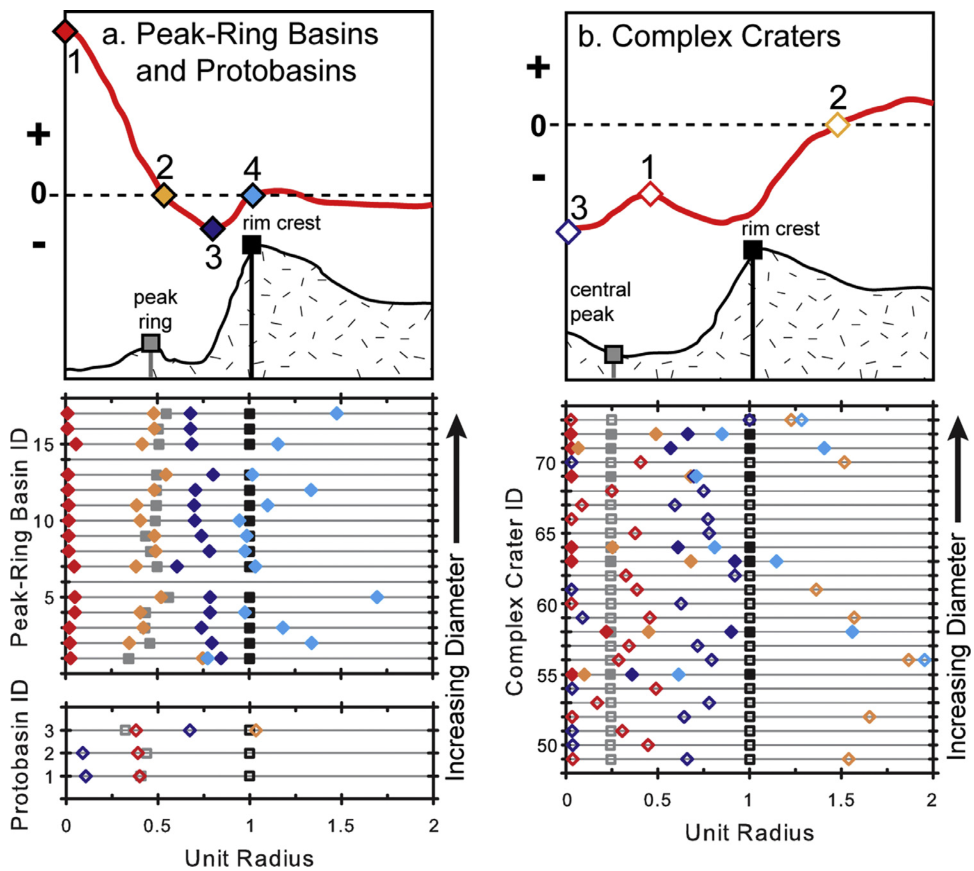

Fig. 5. Locations of the main features of average Bouguer anomaly profiles for peak-ring basins, protobasins, and complex craters. a) Typical Bouguer anomaly profile of a peak-ring basin showing a positive central anomaly and negative anomaly annulus. Diamonds on the profile correspond to the central maximum ("1", red), the first zero crossing ("2", orange), interior minimum ("3", dark blue), and second zero crossing ("4", light blue) (cf. Fig. 2). Directly below the Bouguer anomaly profile is a representative topographic profile of a peak-ring basin, showing the locations of the peak ring (gray square) and the rim crest (black square). Below the profiles are the measured locations of the main features of the Bouguer anomaly profile for 15 peak-ring basins (excludes Coulomb-Sarton and Moscoviense) and 3 protobasins. Also shown are the measured peak ring and rim-crest radii from Baker et al. (2011a). Locations of features are normalized to the rim-crest radii of the basins. Basins are labeled according to their assigned number (IDs) (Table 1) and are arranged by upward increasing rim-crest diameter. Solid symbols represent structures with positive Bouguer anomalies confined to their centers (0.5*R*), while open symbols represent structures without central positive Bouguer anomalies. b) Same as (a) but for the 25 largest complex craters. Solid symbols represent structures with positive Bouguer anomalies confined to their centers (0.5*R*), while open symbols represent structures without central positive Bouguer anomalies. The approximate diameters and corresponding radii of the central peaks for each crater (grey boxes in bottom panel of (d)) were calculated using the relationship of $D_{cp} = 0.259D_r - 2.57$ (units in km) from Hale and Head (1979). (For interpretation of the references to colour in this figure legend, the reader is referred to the web version of this article.)

is highly variable, and typically does not occur near the center of the structure (Fig. 5b). The interior minimum is much more irregular in its location than in peak-ring basins, with a mean value of $0.56 \pm 0.32R$. In some cases, the interior minimum is located near the center of the structure, in others it is near the rim crest. As a result, the first zero crossing is also highly variable and a second zero-crossing is commonly not observed. Sources of variation in the BA signal for complex craters are difficult to parse without more detailed analyses of individual craters. Variations in the response of the lunar interior to impact events depend on projectile properties, impact conditions, and target attributes. Furthermore, pre-existing, subsurface-density structure and post-impact processes (e.g., magmatism) can affect the Bouguer signal, leading to some of the observed scatter.

In order to gain a statistical understanding of the seemingly random BA behavior of complex craters, we assembled a database of 968 BA map grids for structures with rim-crest diameters (D_r) between 20 and 330 km Head et al. (2010). Most of these craters (92%) have $D_r \leq 150$ km and peak-ring basins (degraded or otherwise; See Fig. 6 and Section 5) dominate the sample at $D_r \gtrsim 200$ km. The grids were calculated from the JPL spherical harmonic Bouguer coefficient set 780C8A. To remove the regional signal and to account for the fidelity of the Bouguer solution, the spherical harmonics were band-pass filtered between degrees 50 and 540 using 20-degree cosine tapers at both ends. These model runs were specifically tuned to examine a large suite of the complex craters, down to the transition to simple craters at about 20 km diameter. In particular, a more severe low-degree cutoff does a better job of isolating the typical small Bouguer signals associated with complex craters from larger, longer-wavelength contributions. The reader is referred to discussions in Soderblom et al. (2015), Neumann et al. (2015) and Bierson et al. (2016) for more information on gravity grid production techniques and considerations when analyzing structures at the sizes of complex craters.

Plotted against rim-crest diameter, we examined, *inter alia*, (*i*) the BA at the center of the crater, (*ii*) the maximum BA within the crater, and (*iii*) the minimum BA within the crater (Fig. 7). The scatter in central BAs has a mean of near zero out to $D_r \approx 150$ km (Fig. 7), beyond which a 3rd-order polynomial fit and 50-km diameter intervals in D_r means indicate a systematic positive slope ($\Delta BA/\Delta D_r$) of about 0.4 mGal/km. The maximum BAs (Fig. 7b) show slightly positive interval means, the lower range not statistically separable from zero, out to $D_r \approx 150$ km, beyond which there is a strongly positive trend into the regime of peak-ring basins. The minimum *BAs* (Fig. 7c) exhibit a slightly negative slope in the interval means from $D_r = 20$ km to $D_r \approx 200$ km, but the slope is not

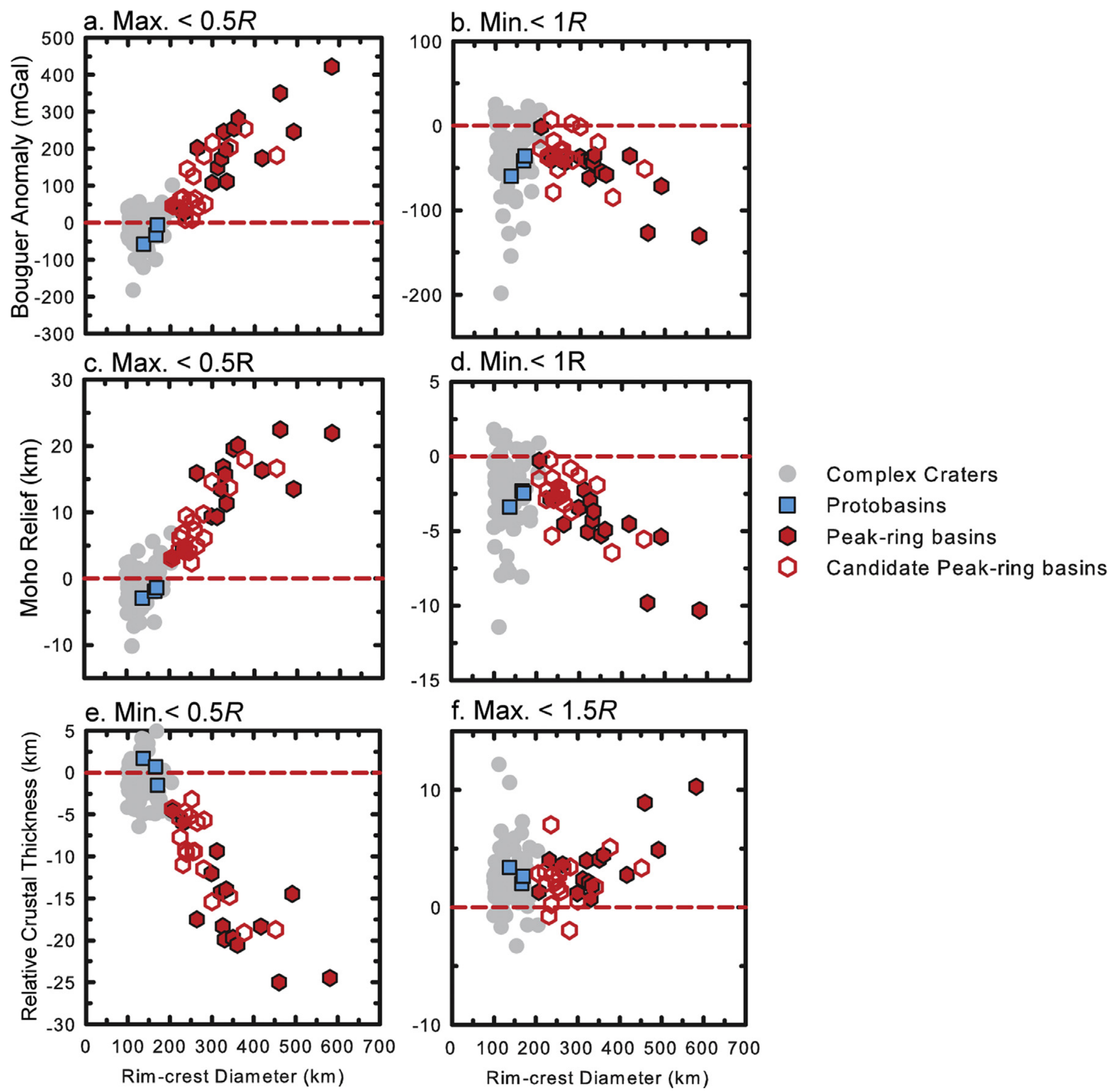

Fig. 6. Maximum and minimum values of the central and interior Bouguer anomaly, Moho relief, and crustal thickness as a function of rim-crest diameter for complex craters (gray circles), protobasins (blue squares), peak-ring basins (solid red hexagons), and candidate peak-ring basins (open red hexagons). (a) Maximum Bouguer anomaly within 0.5*R*. (b) Minimum Bouguer anomaly within 1*R*. (c) Maximum Moho relief within 0.5*R*. (d) Minimum Moho relief within 1*R*. (e) Minimum crustal thickness within 0.5*R*, corresponding to central thinning of the crust for peak-ring basins. (f) Maximum crustal thickness within 1.5*R*, corresponding to an annulus of thickened crust ("crustal annulus") for peak-ring basins. Crustal thickness variations are relative to the average thickness taken at three crater radii (*t*). (For interpretation of the references to colour in this figure legend, the reader is referred to the web version of this article.)

statistically different from zero. Beyond 200 km, the increasingly negative slope mirrors the growing importance with increasing diameter of the negative BA annulus in the outer portions of the structure, as shown in peak-ring basins (Figs. 5a and 6b).

In summary, while complex craters exhibit highly irregular BA behavior, a statistical treatment of a large sample of structures with refined band-pass filtered grids (Fig. 7) reveals that positive central BAs begin to dominate at ∼150 km in rim-crest diameter (Fig. 7a,b). The minimum BAs (Fig. 7c) reveal that the magnitude of the negative annulus begins to increase at $D_r \approx 200$ km, or near the onset of peak-ring basins. Thus, structures in the interval between ∼150 to 200 km are transitional in their BA behavior. Some, like the complex crater Petavius ($D_r = 180$ km) (Fig. 7d), exhibit a somewhat irregular BA high (∼20 mGal) over the center of the crater, including the central peak, and a minor, poorly-developed accompanying negative annulus. Petavius also exhibits floor fractures, possibly associated with an underlying magmatic sill of high density (Schultz, 1976; Jozwiak et al., 2012), which may be affecting the observed positive BA patterns. Other complex craters within this transitional range do not exhibit any central BA highs or negative annuli. Perhaps not coincidentally, the 150- to 200-km diameter range also shows transitions in interior landforms, with the three protobasins (having both a central peak and peak ring) on the Moon occurring at diameters of 137, 166, and 170 km.

Soderblom et al. (2015) recognized a similar transition in central BA. They defined the central BA as the difference in the area-weighted mean BA between a structure's center out to 0.2*R* and an annulus from 0.5 to 1.0*R*. Their analysis of ∼1200 lunar highlands craters from 27 to ∼1000 km in diameter showed a break in slope in the trend of central BA at a diameter of 218 ± 17 km, which was interpreted to represent the onset of mantle uplift at this diameter. Our observations support this interpretation but suggest that the onset of mantle uplift may occur at slightly smaller diameters below 200 km.

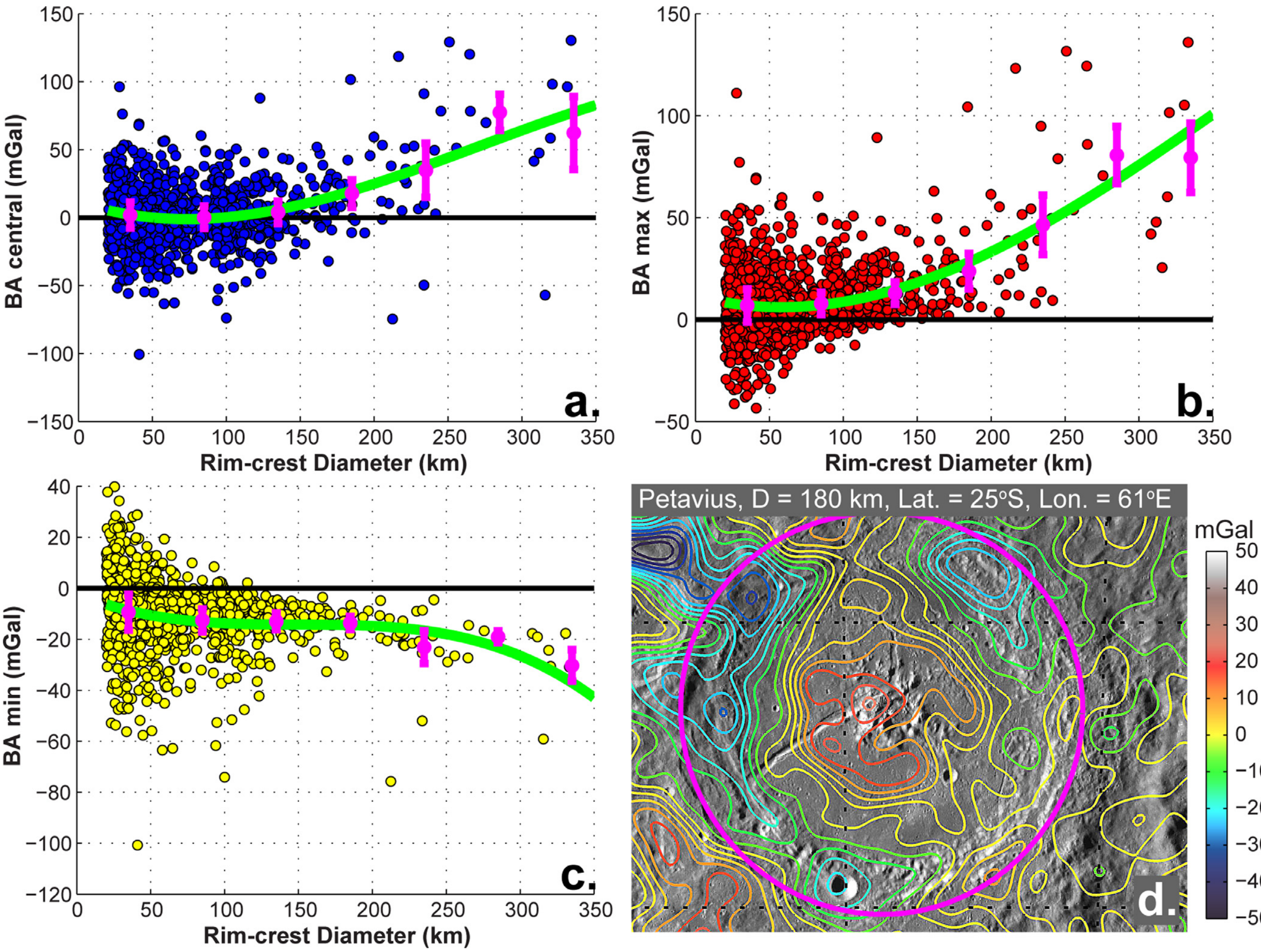

Fig. 7. Bouguer anomalies (BAs) of 968 impact structures plotted against crater rim-crest diameter (D_r). Twenty annular BA means out to one crater radius were obtained; those data were used to generate this figure. (a) The central value ("BA central") is the average of the means of the first two rings out from the crater center. (b) The maximum value ("BA max") is the largest of the annular means. (c) The minimum value ("BA min") is the smallest of the annular means. The green curves are 3rd order polynomial fits to all of the data. Mean values with standard errors are shown (magenta) for 50-km sampling intervals of D_r. (d) Bouguer anomaly contours (5 mGal contour interval) over an LROC wide-angle image of the complex crater Petavius (180 km; 25.39°S, 60.84°E). The magenta circle indicates the average location of the rim crest. (For interpretation of the references to colour in this figure legend, the reader is referred to the web version of this article.)

4. Interpretations of gravity and crustal structure

To help in the interpretation of the trends in Bouguer gravity anomalies, we examined recent global models of Moho relief and crustal thickness from Wieczorek et al. (2013), which are described in Section 2.1. Similar to the gravity anomalies (Fig. 5), we calculated average profiles for Moho relief and crustal thickness and measured the positions and magnitudes of major features in those profiles (Figs. 6c-f, 8, and 9). Because the models by Wieczorek et al. (2013) show that most of the subsurface gravitational signal is the result of relief along the crust-mantle interface, rather than lateral density variations in the crust, profiles of the Moho relief mimic the BA profiles (Fig. 8).

Under these assumptions, several interpretations of the trends in BA trends may be made. The central positive BAs are interpreted to be the result of mantle uplifted in the centers of the basins (Neumann et al., 2015). The perimeter of the central Moho uplift is almost completely enclosed by the peak ring (Fig. 8a). The magnitude of the uplift ranges from 3 km at the smallest peak-ring basin ($D_r = 207$ km) to 22 km at the largest ($D_r = 582$ km) (Fig. 6c). This central Moho relief also corresponds to thinning of the crust relative to the average pre-impact thickness (Fig. 6e); again, this thinning is confined to the interior of the peak ring (Fig. 9a). Magnitudes of this crustal thinning range with increasing diameter from approximately 5 km to 25 km (Fig. 6e). The actual amount of crustal removal implied by the modeled thickness of the crust beneath peak-ring basins may be underestimated because much of the crust interior to the peak ring is expected to be melted during impact-basin formation (e.g., Cintala and Grieve, 1998a,b; Vaughan et al., 2013; Freed et al., 2014), forming kilometers-thick melt sheets mainly confined within the peak ring (e.g., Vaughan et al., 2013). Some complex craters may show several kilometers of Moho uplift (Fig. 6c), but most of those uplifts are not confined to 0.5R (Fig. 8b), as is the case for peak-ring basins.

The negative annulus of the Bouguer-anomaly profile in peak-ring basins is inferred to be the result of depression of the Moho and thickening of the crust outward from the edge of the central mantle uplift (Neumann et al., 1996, 2015; Wieczorek and Phillips, 1998; Melosh et al., 2013). The crustal thickening, or "crustal annulus" (Fig. 10), is typically confined to the region between the peak ring and rim crest (Figs. 8a and 9a). Interior minima of Moho relief are located at a mean value of $0.7 \pm 0.07R$, but this location appears to slightly migrate inward from the rim crest at the largest sizes (Fig. 8a). Ratios of the magnitude of the interior minimum

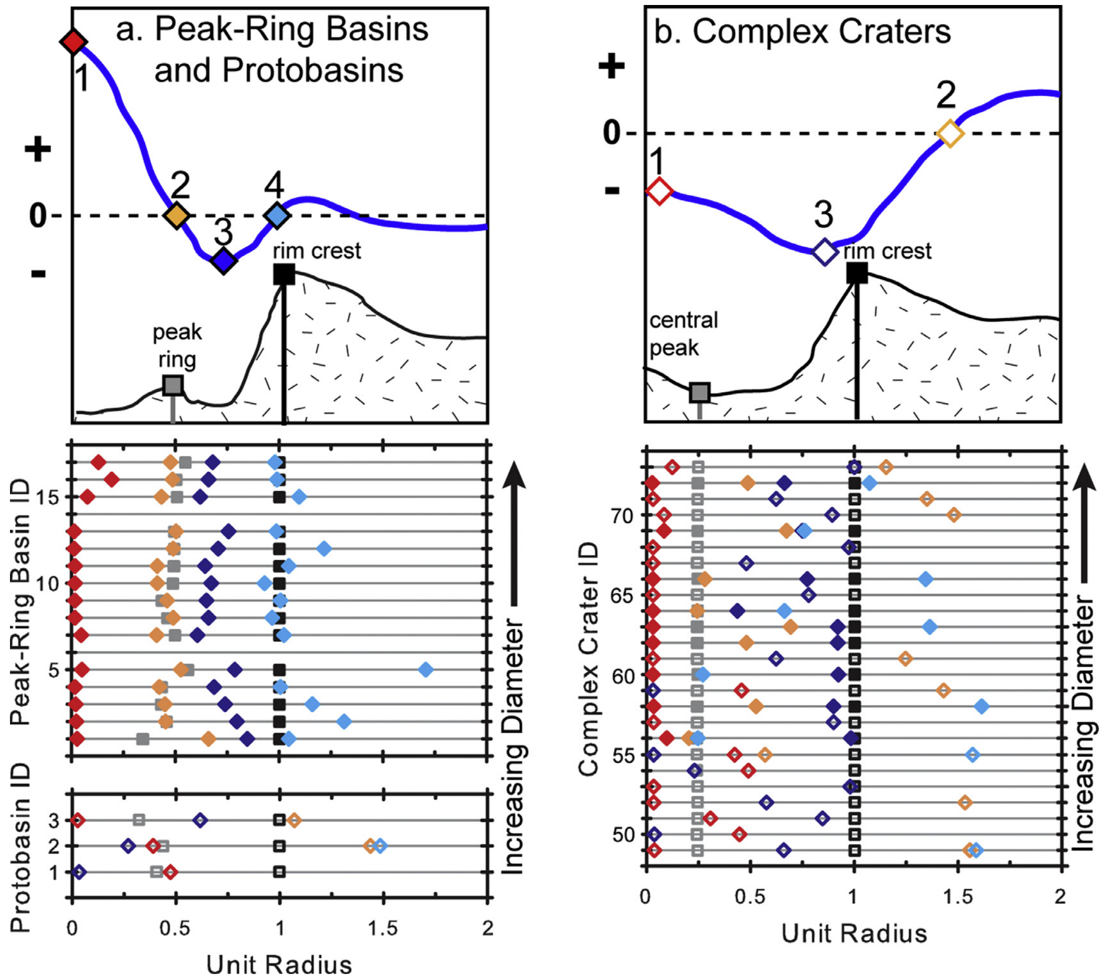

Fig. 8. Locations of the main features of average Moho relief profiles (Wieczorek et al., 2013) for peak-ring basins, protobasins, and complex craters. The figure panels are set up the same as in Fig. 5; please refer to the Fig. 5 caption and text for additional details on measurements and symbols.

of Moho relief to the central maximum may increase slightly with rim-crest diameter from around 0.15 to 0.4, with a mean value for peak-ring basins of 0.28 ± 0.1 (excluding d'Alembert; see above for BAs).

As with gravity anomalies, Moho relief and crustal thickness variations associated with protobasins and complex craters are much more irregular, and do not show the distinctive crustal profiles that occur in peak-ring basins (Figs. 8b and 9b). However, the occurrence of an upturn in central and maximum BAs beginning at $D_r \approx 150$ km (Fig. 7a and b), with positive BAs occurring in some complex craters, suggests the presence of modest uplift of the mantle or deep, denser crustal layers for craters with $D_r \approx 150$ to 200 km. The trend of minimum Bouguer anomalies (Fig. 7c) also suggests that development of a well-defined annulus of thickened crust is mainly associated with the onset of peak-ring basins near 200 km in diameter.

In summary, Bouguer gravity anomalies and models of Moho relief and crustal thickness determined from GRAIL gravity data by Wieczorek et al. (2013) suggest a prominent change in crustal structure near the onset diameter of peak-ring basins (Fig. 10). The data presented here are in good agreement with those of Neumann et al. (2015) and Soderblom et al. (2015) and reveal important additional details not treated previously. The formation of complex craters smaller than about 150 km does not appear to have resulted in any significant uplift of the mantle or deep, denser crustal layers (Fig. 10a). In the transition to peak-ring basins from diameters of ~150 to 200 km, some complex craters begin to show modest uplift of the mantle and/or intra-crustal density boundaries. However, annuli of thickened crust appear to be either minor or non-existent within this transitional diameter range. At the onset diameter of peak-ring basins (~200 km), the Moho in the center of the basin is higher by several kilometers with respect to its pre-impact level, and there is an annulus of crustal thickening, whose maximum lies approximately midway between the peak ring and rim crest (Fig. 10b). The central mantle uplift has a diameter nearly equal to that of the peak ring and is associated with thinning of the crust in this region. The central mantle elevation and the thickness of the crustal annulus are even greater in magnitude at the largest peak-ring basins (Fig. 10c), producing substantial crustal thinning below the centers of these basins and increasing in crustal thickness between the peak ring and rim crest.

5. Recognition of degraded peak-ring basins

One of the most significant results from lunar gravity data has been the recognition that, although the topography of a basin degrades with time through a number of surficial processes, the subsurface structure may still be largely preserved (Neumann et al., 1996, 2015). Since peak-ring basins have distinctive Bouguer-anomaly profiles, we surveyed existing crater databases on the Moon to search for candidate peak-ring basins that have degraded to the point where their interior ring structures are currently not visible. From a global survey using the crater catalog of Head et al. (2010) and a global GRAIL- and LOLA-derived Bouguer

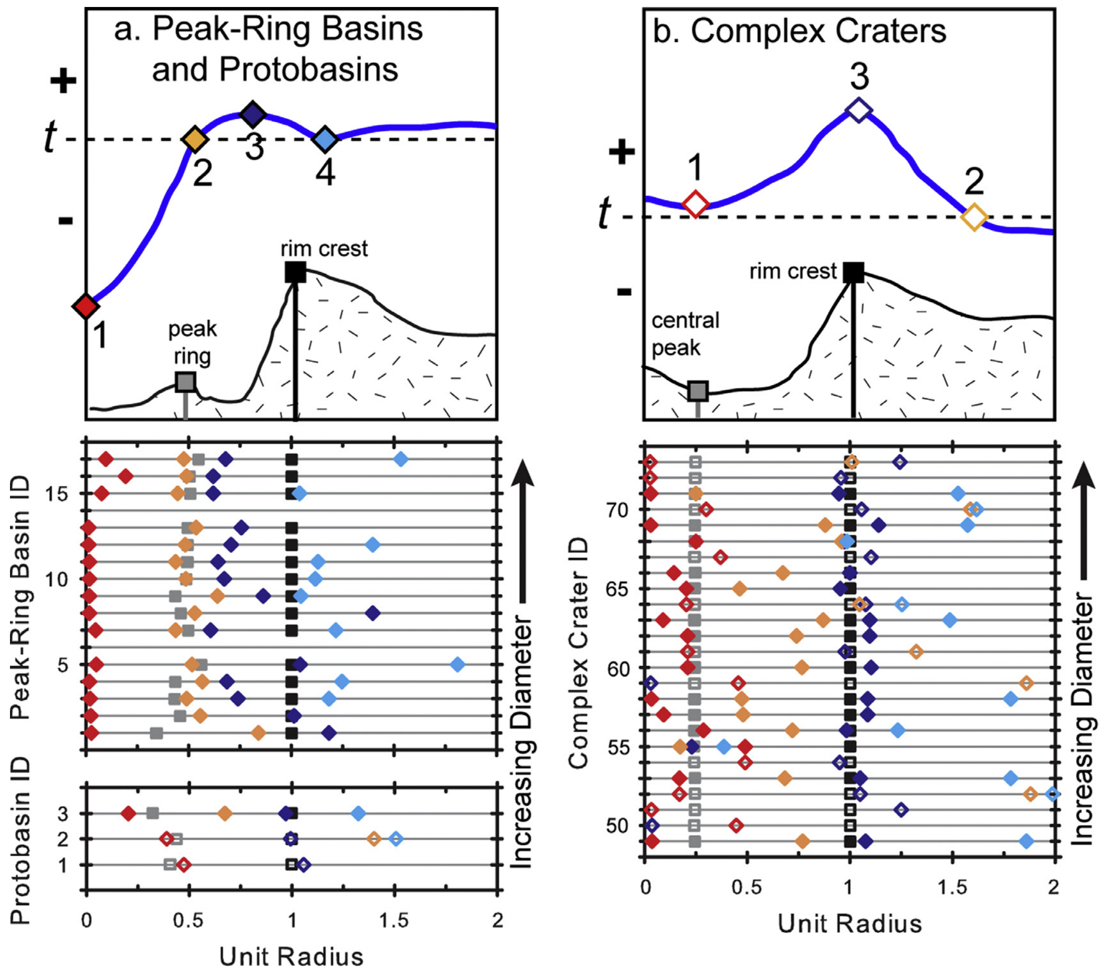

Fig. 9. Locations of the main features of crustal-thickness profiles (Wieczorek et al., 2013) for peak-ring basins, protobasins, and complex craters. Crustal thickness variations are relative to the average thickness taken at three crater radii (t). The figure panels are set up in a similar manner as in Fig. 5, with the exception that a central minimum is calculated and labeled as point "1" in (a) and (d), and an annular maximum is calculated and labeled as point "3"; please refer to the Fig. 5 caption and text for additional details on measurements and symbols.

gravity-anomaly map expanded from degrees 7 to 450, we identified 18 basins with preserved rim crests that have diameters and Bouguer-anomaly trends similar to peak-ring basins cataloged by Baker et al. (2011a) and presented here (Table 1). Since the rim-crest diameters of these 18 basins are within the diameter range of peak-ring basins, and all are larger than that of the largest complex craters on the Moon (205 km, Humboldt), initial morphometric classification would define these impact features as candidate basins. Definitive morphological evidence of two or more rings [the original definition of a basin (Hartmann and Kuiper, 1962)] is lacking, as examination of their surface morphology shows that all of the candidate peak-ring basins have had their interiors obscured by superposed impact craters and/or mare resurfacing, both of which we infer to have removed evidence of their interior peaks. However, the occurrences of strong, circular, positive BAs in the centers of these basins along with surrounding annuli of negative anomalies provide compelling evidence that these impact structures are true peak-ring basins. Plots of the spatial locations of major features in average gravitational profiles of candidate peak-ring basins using the methods outlined above are very similar to those of peak-ring basins (Fig. 11). Furthermore, the magnitudes of central maximum and interior minimum anomalies of these basins plot along the trends of peak-ring basins (Figs. 3 and 6).

Should these 18 candidates be true peak-ring basins, then the number on the Moon increases by more than a factor of two to 34 (not including Coulomb-Sarton, see below), with the number of peak-ring basins per unit area on the Moon growing to 8.9×10^{-7} per km^2. This is still about a factor of two fewer than the number of peak-ring basins per unit area on Mercury (1.5×10^{-6} per km^2; $N = 110$) (Baker et al., 2011b; Baker and Head, 2013). This difference in surface density of peak-ring basins is still unclear, but may result from differences in the mean impact velocity and cratering rate on the two bodies (Baker et al., 2011b; Baker and Head, 2013). Several ringed basins proposed by Pike and Spudis (1987) (Amundsen-Ganswindt, Oppenheimer, Fermi, Schickard, Balmer-Kapteyn, Pasteur, Compton, and Landau) are included in our list of candidate peak-ring basins.

There are also eight structures within the diameter range of peak-ring basins with Bouguer gravity-anomaly patterns that were too irregular or dissimilar to those in known peak-ring basins, as assessed here, to be so classified (Table 2). All of these structures lack both well-defined, circular, positive BAs located near their centers and associated negative annuli. Positive anomalies that do occur within these basins are highly irregular and are usually located off-center.

In addition to the candidate peak-ring basins listed in Table 1, Neumann et al. (2015) identified six others — Wegener-Winlock, Orientale Southwest, Bartels-Voskresenskiy, Aestuum, Fowler-Charlier, and, Crüger-Sirsalis—that were suggested to be candidate peak-ring basins. Three of these basins—Wegener-

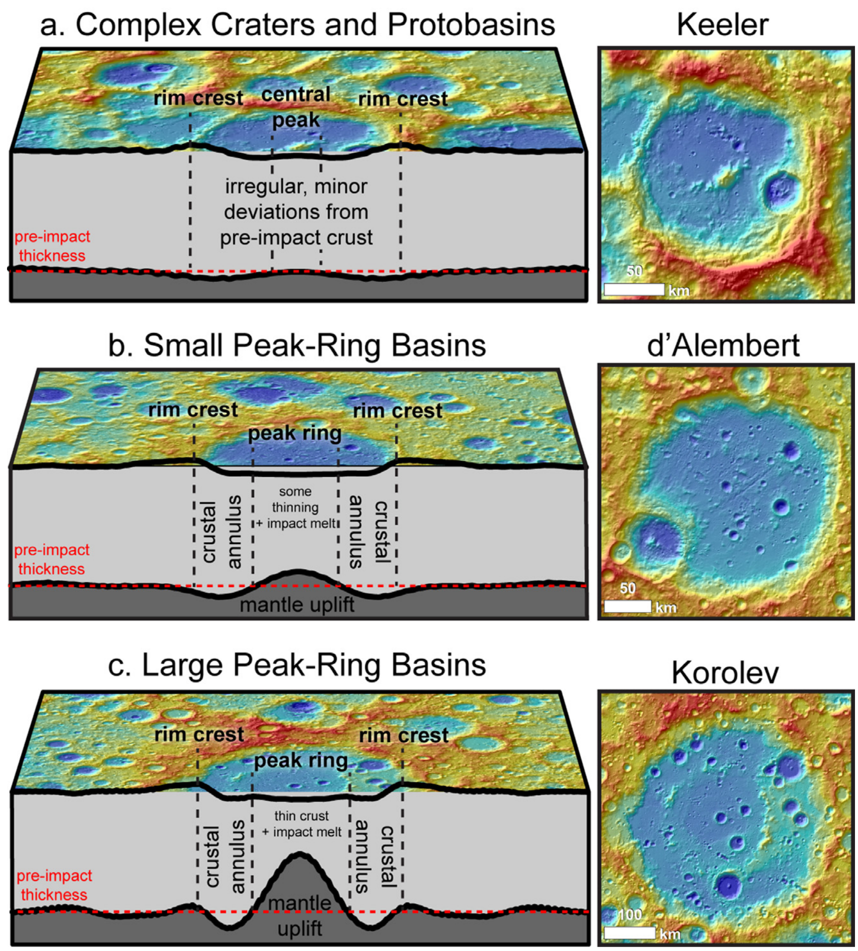

Fig. 10. Schematic diagram of the interpreted changes to the crust-mantle boundary that occur in the transition from complex craters to peak-ring basins on the Moon. (a) Complex craters and protobasins show irregular, minor to no relief along the crust-mantle boundary relative to the pre-impact crust (dashed red line). Modest central uplift of the mantle or deep, denser crustal layers occurs in some complex craters starting near 150 km in diameter. Shown is a LOLA topographic map of Keeler crater (161 km; 9.70°S, 161.96°E). (b) The onset of peak-ring basins (~200 km) is marked by a few kilometers of uplift of the Moho that is spatially confined to the inside of the peak ring. A slight thickening of the crust ("crustal annulus") is observed from the outward edge of the mantle uplift to near the location of the rim crest. Shown is a LOLA topographic map of the peak-ring basin, d'Alembert (232 km; 51.05°N, 164.84°E). (c) The Moho is uplifted by as much as 20 km relative to the pre-impact level in the centers of the largest peak-ring basins; this uplift is also spatially confined to the interior of the peak ring. The magnitude of the thickness of the crustal annulus also increases for the largest peak-ring basins. Shown is a LOLA topographic map of the peak-ring basin, Korolev (417 km; 4.44°S, 157.47°W).

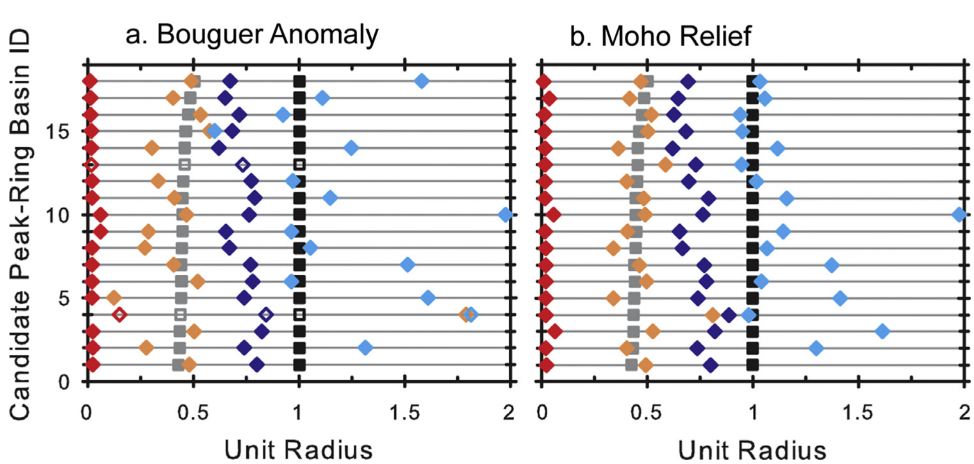

Fig. 11. Locations of the four major features in average profiles of Bouguer gravity anomalies (a) and Moho relief (b) for 18 candidate peak-ring basins on the Moon. The plots were produced as described in Figs. 5a and 8a. Solid symbols in (a) represent structures with positive Bouguer anomalies confined to their centers (0.5*R*), while open symbols in (a) represent structures with central maximums in the Bouguer anomaly that are not positive. Peak-ring diameters and corresponding radii (grey boxes) were estimated using a power law relationship between peak-ring diameter (D_{pk}) and rim-crest diameter (D_r) from Baker et al. (2011a): $D_{pk} = 0.14 D_r^{1.21}$. Distances are normalized to one crater/basin radius. Candidate peak-ring basins no longer preserve an interior peak ring, however they have measureable rim-crest diameters within the range of known peak-ring basins (Baker et al., 2011a) and Bouguer gravity and Moho relief patterns that are very similar to known peak-ring basins (compare plots to those in Figs. 5a and 8a). These observations, along with measureable rim crests but degraded character, provide strong evidence that candidate peak-ring basins are most likely true peak-ring basins that have not preserved their interior peak rings due to resurfacing, superposed impacts, proximal weathering, or other degradation processes.

Table 2
Basins with measurable rim-crest diameters that are within the diameter range of peak-ring basins, but which possess Bouguer gravity-anomaly patterns that are too irregular or dissimilar to qualify as candidate peak-ring basins.

Name[a]	Latitude	Longitude[b]	D_r	Reference[c]
Aestuum**	11.43	−9.91	330	Frey (2011)
Orientale Southwest**	−28.13	−108.52	276	Head et al. (2010)
Janssen	−44.35	40.64	230	Head et al. (2010)
Clavius	−58.69	−14.77	221	Head et al. (2010)
Keeler West**	−10.11	156.84	219	Head et al. (2010)
Rupes Recta**	−22.49	−7.05	212	Head et al. (2010)
Galois	−14.11	−152.65	210	Head et al. (2010)
Wegener-Winlock*	40.23	−108.36	205	Head et al. (2010)

[a] Names given are approved by the IAU except when followed by an asterisk (*). Names with a single asterisk are from previous catalogs (Frey, 2011). Names with two asterisks are provisional names from Neumann et al. (2015).
[b] Latitude and longitudes are from the tables in the diameter reference. Longitudes are positive eastward and negative westward.
[c] Diameters and coordinates are from tables or databases in the given references: Frey (2011), Table 1; Head et al. (2010), online crater database (http://www.planetary.brown.edu/html_pages/LOLAcraters.html).

Winlock, Orientale Southwest, and Aestuum—are listed in Table 2 here as structures with measureable rim-crest diameters but with Bouguer-anomaly patterns that are notably irregular or dissimilar in profile to the known peak-ring basins. All three of these structures have been influenced by the structures of nearby impact basins or mare lavas, making interpretation of their gravity characteristics more difficult. Orientale Southwest is near the rim of the Orientale basin and possesses an irregular central positive anomaly, but its negative annulus is much more subdued than those of other peak-ring basins. The Bouguer-anomaly pattern of Wegener-Winlock is convolved with the gravity signature of Coulomb-Sarton and could not be confidently distinguished or characterized using the techniques employed here. Aestuum's central BA is too broad for its rim-crest diameter, a characteristic likely influenced by substantial interior resurfacing by mare material. Neumann et al. (2015), however, using a slightly different method of analysis, noted the strong BA contrasts in the interiors of these basins. These contrasts appeared aligned with the general BA trend for peak-ring basins and justified the classification of Wegener-Winlock, Orientale Southwest, and Aestuum as candidate peak-ring basins. In addition, while not meeting our criteria for possessing measurable topographic rim crests, Neumann et al. (2015) suggested that Bartels-Voskresenskiy, Fowler-Charlier, and, Crüger-Sirsalis be included as candidate peak-ring basins based on their well-defined gravity signatures; those three structures, however, do not meet our criteria for possessing measureable topographic rim crests. Other topographic depressions without discernable rim crests were also identified from gravity by Neumann et al. (2015) to be impact basins, forming a more complete list of such features than can be made using surface morphology alone.

A unique example of one of the candidate peak-ring basins is the 377-km diameter Amundsen-Ganswindt basin (Fig. 12), which has been largely superposed by the comparably sized Schrödinger basin and other smaller impact craters. As a result of the formation of Schrödinger, the interior topography of Amundsen-Ganswindt is nearly completely obscured, with no strong topographic evidence for a peak ring (Fig. 12a). Remarkably, a ∼250 mGal, circular, central positive Bouguer gravity anomaly is still observed in Amundsen-Ganswindt, which spatially extends into the southern wall and floor of Schrödinger basin (Fig. 12b). The average profile of the BAs in Amundsen-Ganswindt (Fig. 12c) is nearly identical to those of other large peak-ring basins on the Moon (Fig. 2b). The regularity and strength of the central BA and, by inference, Moho relief imply that the subsurface structure beneath

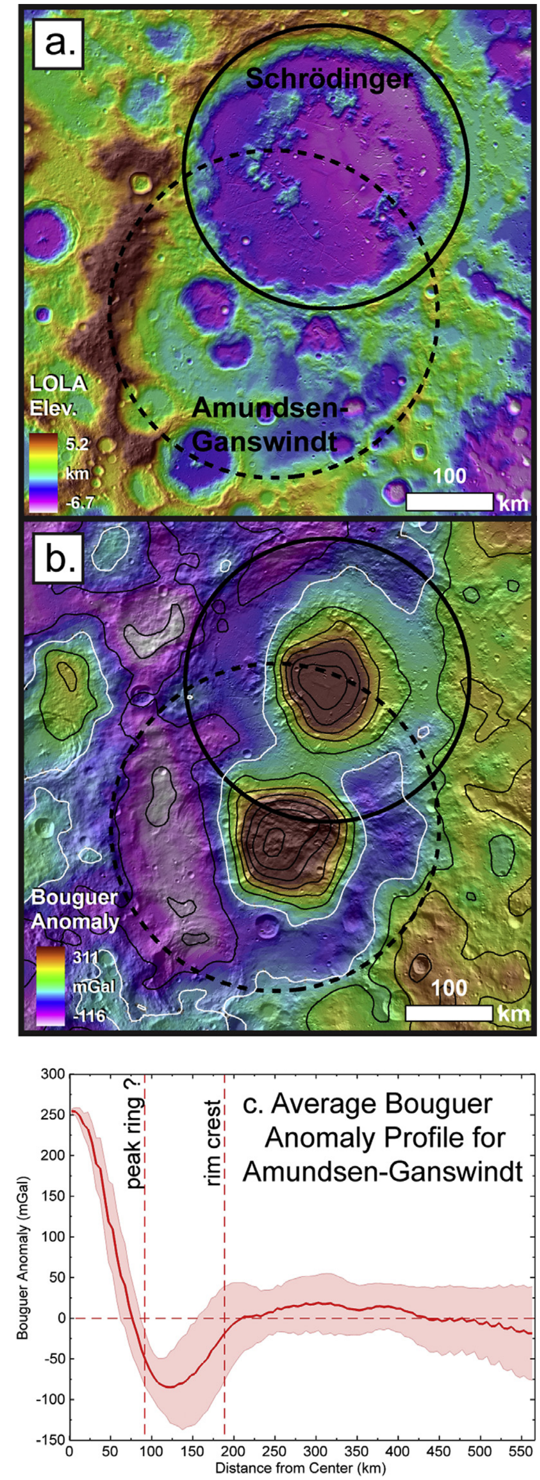

Fig. 12. An example of a candidate peak-ring basin, Amundsen-Ganswindt (377 km; 80.59°S, 124.36°E), which has had its interior obscured by the Schrödinger impact event. (a) LOLA gridded topography overlain on a LOLA gridded hillshade map. Amundsen-Ganswindt's interpreted rim-crest outline is the dashed circle, and the Schrödinger basin is outlined by the solid circle. Topographic evidence of a peak ring in Amundsen-Ganswindt has been obscured by the younger Schrödinger basin and smaller impacts. (b) GRAIL Bouguer gravity anomaly map of the two basins, expanded from degrees 7 to 450 and showing 25 mGal contour intervals (0 mGal is in white). Amundsen-Ganswindt has a well-defined 250 mGal central Bouguer anomaly that does not appear to have been disrupted by the Schrödinger impact event. Surrounding the central positive anomaly is a negative annulus, which is interpreted to have been disrupted by mantle uplift in the center of Schrödinger. (c) Average Bouguer anomaly profile of Amundsen-Ganswindt, showing features identical to those of less degraded peak-ring basins (cf. Fig. 2b).

Amundsen-Ganswindt was not substantially modified during the Schrödinger impact event. This implies that deformation of the deep crust resulting from collapse to form Schrödinger must not have extended to radial distances much farther than the uplifted rim crest of the transient cavity (at about 100 km from the center of the structure; see supplementary Table S5). Examples like these, as revealed by the GRAIL dataset, have important implications for understanding and constraining the pervasiveness and types of target-weakening mechanisms that are necessary for collapse of the transient cavity (Kenkmann et al., 2013).

We also identified one peak-ring basin in the catalog of Baker et al. (2011a) that should be reclassified as a multi-ring basin on the basis of GRAIL gravity data. The Bouguer gravity profile of Coulomb-Sarton, which was classified as the most uncertain peak-ring basin in the catalog of Baker et al. (2011a), has a much broader BA than predicted from its topographically measured ring and rim-crest locations. The central positive BA extends outward almost to the originally defined rim-crest in Coulomb-Sarton (158 km radius), suggesting that the "rim crest" is actually most analogous to a peak ring. From the shape of the negative annulus and extent of the crustal annulus, we assign a radius of approximately 330 km for Coulomb-Sarton, which is twice as large as measured by Baker et al. (2011a). This is greater than that of the largest peak-ring basin (Freundlich-Sharonov) on the Moon, and the implication of at least three rings indicates that Coulomb-Sarton could be a multi-ring basin.

6. Implications for models of mascon and basin-ring formation

6.1. Mascon formation

Mascons on the Moon are characterized by central positive free-air anomalies, and most basins >300 km in diameter on the Moon are associated with mascons (e.g., Dombard et al., 2013). Central, positive free-air anomalies associated with lunar-mascon basins have been most commonly interpreted to result mainly from the super-isostatic uplift of the mantle during basin formation (Wise and Yates, 1970; Neumann et al., 1996; Wieczorek and Phillips, 1999; Namiki et al., 2009). Recent work, however, suggests that mascons are formed from the combined effects of short-term impact processes and longer-term post-impact isostatic adjustments of the basin (Andrews-Hanna, 2013; Melosh et al., 2013; Freed et al., 2014). Melosh et al. (2013) and Freed et al. (2014), in a more detailed study, conducted numerical simulations of two basin-forming events and used the final states of the basins as initial conditions to model their responses to post-impact viscoelastic, isostatic adjustments. The predicted free-air anomaly profiles of the basins were calculated from the models and compared with GRAIL gravity profiles, showing good agreement. Immediately post-impact, the general pattern of the free-air anomaly profile is predicted to form by the presence of a sub-isostatic ring of thickened crust and a thinning of the crust in the center of the basin. The thinned crust is due to removal by excavation and a return to approximately an equilibrium (∼isostatic) state of the crust-mantle boundary beneath the basin. The free-air anomaly profile is predicted to be negative in the center of the basin due to basin excavation and the lower density of heated material; this contrasts with early hypotheses that suggested that super-isostasy of the central mantle uplift is a feature produced during the impact event (Neumann et al., 2006; Wieczorek and Phillips, 1999). Instead, models by Melosh et al. (2013) and Andrews-Hanna (2013) indicate that current super-isostasy observed in mascons is formed by post-impact isostatic adjustment of the basin. Cooling of the impact-heated mantle beneath the basin creates a pressure gradient from its exterior to interior, driving viscoelastic flow toward the basin center and uplifting the annulus of thickened crust

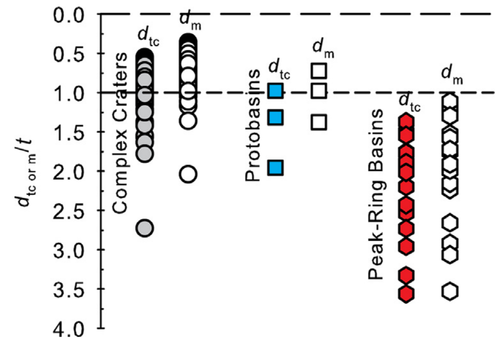

Fig. 13. Ratios of the maximum depth of the transient cavity (d_{tc}) or maximum depth of melting (d_m) relative to the average crustal thickness (t) for complex craters (circles), protobasins (squares), and peak-ring basins (hexagons). See text for a description of how these values were calculated. The transient cavities of peak-ring basins extend into the mantle, with d_{tc}/t ratios > 1.5. Most complex craters and protobasins have d_{tc}/t ratios < 1.5, with a few having larger ratios. Since the depth of melting is slightly smaller than the depth of the transient cavity, the d_m/t ratios for peak-ring basins are smaller than their d_{tc}/t ratios. The maximum depth of melting is near equal to the crustal thickness at the onset of peak-ring basins; the maximum depth of melting for most complex craters and protobasins is confined to the upper and lower crust.

and the basin floor (Andrews-Hanna, 2013; Melosh et al., 2013). Taken together, the important mascon-forming processes in these models are predicted to be (1) sufficient transient crater and melt depth to quickly return the Moho to a quasi-equilibrium (∼isostatic) position during the impact event; (2) sufficient thickening in the crustal annulus (resulting from loading by ejecta and collapse of the transient cavity wall) to create the necessary upward driving stresses; (3) sufficiently high mantle temperatures to allow flexural adjustments post-impact; and (4) mechanical coupling between the heated, then cooled, central portions of the basin and the thickened outer ones.

GRAIL gravity data show that many peak-ring basins down to ∼250 km in diameter harbor mascons, defined by the presence of positive central free-air anomalies (Fig. 3). This evidence supports the idea that the mascon driving processes, as predicted in current models (Andrews-Hanna, 2013; Melosh et al., 2013; Freed et al., 2014) and described above, continue across the transition in size and morphology from multi-ring basins down to peak-ring basins. Furthermore, the lack of a positive free-air anomaly signature below a rim-crest diameter of ∼250 km (that is, predominantly complex craters) suggests that at least one of the four major processes driving mascon formation listed above ceases or becomes ineffective below this size. However, Bouguer anomalies of a large sample of craters (Fig. 7) show that modest mantle uplift or uplift of deep, denser crustal layers occurs at diameters as small as 150 km, suggesting that vestiges of the mascon formation processes extend down into the complex-crater regime (see also Soderblom et al., 2015). On the other hand, development of a collar of thickened crust, which is crucial for the development of mascons in current models (Andrews-Hanna, 2013; Melosh et al., 2013; Freed et al., 2014), appears to be associated with the onset diameter of peak-ring basins ($D_r \approx 200$ km). Also, the interval of $D_r = 150$ to 200 km is a transitional regime and not all impact structures exhibit such stunted mascon formation; this is obvious from the scatter in the central BAs (Fig. 7a) in this diameter interval.

One of the important factors in mascon formation is the involvement of the mantle and impact melting in uplifting the Moho to a transient state of equilibrium during the impact event. The degree of involvement of the mantle during impact formation can be estimated if we compare the ratio of the depth of the transient cavity (d_{tc}) to the pre-impact crustal thickness (t) for complex craters, protobasins, and peak-ring basins (Fig. 13). The depth of the transient cavity was determined by assuming $d_{tc} \approx 1/3D_{tc}$ (Dence, 1973; Melosh, 1989, p. 78), where D_{tc} is the diameter of the transient cavity. D_{tc} was estimated using the rim-crest diameters (D_r) of Baker et al. (2011a) and Baker and Head (2013) and the crater scaling relationship of $D_{tc}=0.758(D_{sc})^{0.079}(D_r)^{0.921}$ from Holsapple (1993), where D_{sc} is the simple-to-complex transition diameter on the Moon (18.7 km, Pike (1988)). A d_{tc}-D_{tc} ratio of 1/3 is in agreement with studies of small impact craters (Melosh, 1989, p. 78) and numerical simulations of large impact basins (e.g., Turtle et al., 2005; Christeson et al., 2009). Potter et al. (2012) recently determined relationships between the radius of the transient cavity (r_{tc}) and the radius of the crustal annulus (r_{ca}) for numerical simulations of lunar impact basins. These relationships are given as $r_{tc} = 5.12{r_{ca}}^{0.62}$ for an early, high-temperature profile of the crust and mantle and $r_{tc} = 4.22{r_{ca}}^{0.72}$ for a late, low-temperature profile. The high temperature profile assumed a crustal and upper mantle thermal gradient of 10 K/km, mantle temperatures at the solidus between 150 and 350 km, and a constant temperature of 1670 K for the deeper mantle. The low-temperature profile assumed a crustal gradient of 10 K/km, mantle temperatures below the solidus between 300 and 500 km, and a deep mantle temperature of 1770 K (Potter et al., 2012). Using our radii of internal minima of Moho relief (Fig. 8) and average of the results obtained for the two temperature profile relationships of Potter et al. (2012), we calculated transient cavity radii and diameters that had differences of only 13% from those calculated using the scaling of Holsapple (1993). The diameters of Potter et al. (2012) were systematically larger than those determined from the equation of Holsapple (1993). Since these calculations are in close agreement, and since we are examining both craters and basins for which the crust-mantle temperature profiles at the time of their formation are poorly constrained, we chose here to use the Holsapple (1993) scaling. The pre-impact crustal thickness is taken as the average crustal thickness at 3 radii from the center of the crater.

We find that all peak-ring basins have transient cavities that extend into the mantle to depths of ~1.5 to 3.5 times the pre-impact crustal thickness (Fig. 13). The complex craters treated here generally have d_{tc}/t values that are less than 1.5, but a few examples overlap with peak-ring basins. It is clear from Fig. 13 that, at the sizes of peak-ring basins, there is substantial interaction between the transient cavity and the mantle. The transient cavities of large complex craters are largely confined to the lower crust, but with depths that are also predicted to extend into the mantle. These ratios are consistent with observations of the Chicxulub impact basin, which is inferred to have had a d_{tc}/t value near 1.0 (Christeson et al., 2009). Chicxulub is a terrestrial multi-ring basin (D_r ~200 km) (Morgan et al., 2002) that, while possessing a small central Moho uplift and outward crustal thickening, has a subsurface structure distinctly different (Christeson et al., 2009) from those of lunar peak-ring basins. This is not surprising and could be due to a number of factors including differences in target properties and impactor velocities.

Also plotted in Fig. 13 are the ratios of maximum depth of melting (d_m) to t. The maximum depth of melting was calculated using the relationship of $d_m = 0.064{D_{tc}}^{1.29}$ from the lunar melt-scaling relationships of Cintala and Grieve (1998a,b). The Cintala and Grieve (1998a,b) relationship assumes a chondritic impactor impacting vertically into an anorthositic target (Cintala and Grieve, 1998a,b). While in close agreement with other models estimating the volume of impact melt (Pierazzo et al., 1997; Barr and Citron, 2011; Abramov et al., 2012), the resulting impact-melt volumes can be reduced by approximately 20% at the most probable impact angle of 45° (Pierazzo and Melosh, 2000). Assuming a spherical geometry, this translates to a reduction of approximately 5 to 10% in radius of the melted zone, or maximum depth of melting (Pierazzo et al., 1997). Therefore, the maximum depths of melting determined for vertical impacts using the estimates of Cintala and Grieve (1998a,b) are assumed to be reasonable estimates for the purposes of this paper.

The d_m/t ratios between complex craters and peak-ring basins are even more distinct than their d_{tc}/t ratios. The onset of peak-ring basins occurs at a d_m/t ratio of near 1.0, with most complex craters having ratios <1.0. Based on these crater-scaling arguments (Fig. 13), it is clear that the interaction between the transient cavity, depth of melting, and mantle becomes more enhanced at the onset of peak-ring basins. The onset of peak-ring basins also corresponds to the initiation of substantial mantle uplift and formation of a thick crustal annulus (Figs. 5 and 8) and is near the onset of mascons (~250 km). This supports current models (Andrews-Hanna, 2013; Melosh et al., 2013; Freed et al., 2014) that demonstrate that all of these processes are inter-related and important in the development of mascon basins on the Moon. Below a diameter of ~250 km, the impact process is not sufficient to produce the requisite conditions (annulus of thickened crust, uplift of hot mantle and enhanced thermal gradients, and impact melting) needed for mascons to form. However, vestiges of mascon formation (e.g., mantle uplifts) appear to occur down to diameters of ~150 km (Fig. 7a). For these smaller craters we are left with a rich, multidimensional parameter space to explore with future modeling with a plethora of lunar data sets. Further numerical modeling of impact craters within the size range of peak-ring basins and complex craters should further elucidate the details of the process of mascon formation on the Moon.

6.2. Basin-ring formation

The occurrence of mascons down to diameters near the onset of peak-ring basins on the Moon suggests that the processes of mascon formation are disconnected from the number of basin rings formed. However, the very strong correlation between the diameter and onset of Moho uplift and the diameter and onset of the peak rings (Fig. 8a) is highly suggestive that the two are intimately linked. Large vertical uplifts are predicted to occur in numerical simulations of peak-ring basin-sized impact events (e.g., Collins et al., 2002; Ivanov, 2005; Baker et al., 2016). In all the models, the central portions of the basin begin to uplift before the final diameter of the transient cavity is obtained. Most often, the central uplift is modeled to overshoot the rim crest and collapse back downward and overturn on inwardly collapsing wall blocks to produce a peak ring. Advanced numerical simulations of lunar impact basins in the size range analyzed here are sparse (Baker et al., 2016), but should be a focus of future research to evaluate reasonable model parameters for producing peak rings, uplift of the Moho, and their potential linkages. It is also possible that the huge central vertical uplifts suggested from these simulations may act to drive the upward rotation of centro-symmetric, inwardly collapsing walls of the transient cavity to form peak rings in a fashion hypothesized in a conceptual geological model by Baker et al. (2016). In that hypothesis, peak rings are formed by the inward and upward rotation of walls of the transient cavity, without the requirement of an overheightened central peak. Inward displacement of the transient cavity walls should be limited by convergence with the lateral extent of the central uplift, explaining the correlation between peak-ring diameter and diameter of central Moho relief. In both models, the formation of peak rings is predicted to result from the interaction between inwardly collapsing wall material and the huge central, vertical uplift that occurs during basin formation. Our data from GRAIL provide additional evidence in support of these predictions, particularly the central, deep-seated vertical deformation that must occur during basin formation. Differences in style of transient cavity collapse and final morphometry of the basin should be affected by the target strength and transient weakening mechanisms assumed in the models (Wünnemann et al., 2005; Morgan et al., 2011).

What are the implications for multi-ring basin formation? If peak-ring basins are precursors to multi-ring basins, where other rings are formed in addition to the rim-crest and the peak ring, then it is possible to use Bouguer gravity anomalies to determine which ring of a multi-ring basin may be most equivalent to the peak ring. For example, gravity data from previous work (e.g., Neumann et al., 1996; Namiki et al., 2009) show that the central BA of Orientale is confined to within the Inner Rook ring. Recent results from GRAIL (Zuber et al., 2016) and numerical simulations of Orientale (Potter et al., 2013; Johnson et al., 2016) support this observation and further show that the anomaly is mostly confined within the Inner Depression and likely represents the extent of the excavation cavity. These observations, along with geological evidence (Head, 1974, 1977, 2010; Nahm et al., 2013) suggest that the Inner Rook ring is most equivalent to the peak ring. The Outer Rook and Cordillera rings are emplaced outward from the peak ring as through-crustal faults resulting from the flow of warm weak material at depth (Potter et al., 2013; Johnson et al., 2016). Conducting similar analyses of multi-ring basins on the Moon using GRAIL gravity data, as largely completed by Neumann et al. (2015), should help to constrain the peak-ring equivalents in other multi-ring basins, including more degraded examples, providing important constraints for models of ring formation in large impact events.

7. Conclusions

With the improved spatial resolution of the gravity field of the Moon provided by GRAIL, it is now possible to confidently link gravity anomalies produced by subsurface mass variations with surface morphology. Here, we build on the analysis of Neumann et al. (2015) and focus on assessing the three-dimensional structural evolution of impact features in the transition from complex craters to peak-ring basins. Like the morphometric trends in this transition (Baker et al., 2011a, 2012), we find that substantial changes in gravity and crustal structure occur near the onset of peak-ring basins. Complex craters below ∼150 km in diameter show irregular Bouguer gravity-anomaly (BA) profiles, with variations that are not clearly linked to surface landforms such as central peaks. Uplift of the Moho and crustal thickening are therefore interpreted to be non-existent or very minor at these crater sizes. Beginning at a diameter of ∼150 km, central positive BAs are observed within some complex craters but well-developed negative annuli do not appear until a diameter of ∼200 km. These results imply that some complex craters in the transitional diameter range of ∼150 to 200 km show modest mantle uplift but with no or very minor annuli of thickened crust. In contrast, peak-ring basins from their onset are marked by very regular BA patterns, including a central positive anomaly that has a diameter near that of the peak ring diameter (∼0.5R, where R is the radius of the basin rim crest) and a surrounding negative anomaly annulus with a minimum at ∼0.75R. Crustal models suggest that these BA patterns correspond to a central uplift of the Moho between ∼3 to 22 km and an annulus of crustal thickening of ∼1–10 km relative to the pre-impact level. Further, our data indicate that mascon formation extends down to a diameter of ∼250 km, or near the onset of peak-ring basins. The processes important to mascon formation must therefore operate across the multi-ring basin to peak-ring basin transition and are apparently disconnected from the number of basin rings formed. The lack of mascons associated with structures under ∼250 km in diameter suggests that at least one of the processes important to mascon formation ceases or is less effective near and below this diameter and in the transition from peak-ring basins down to complex craters. Vestiges of mascon formation, including uplifted mantle, however, may persist to diameters as small as 150 km. This transition is shown to correlate with the disappearance of an annulus of interpreted crustal thickening; both transient cavity and impact-melt zones are largely confined to the crust for structures below this transition diameter.

We also identified 18 structures that have measureable rim-crest diameters and Bouguer-gravity signatures very similar to those of peak-ring basins, but degradational processes have removed morphological evidence of their peak rings. Should these be true peak-ring basins, then they would raise the total number of peak-ring basins on the Moon to 34, doubling the number previously reported. On the basis of its anomalously large, Bouguer-gravity dimensions, we suggest that Coulomb-Sarton be re-classified as a possible multi-ring basin.

Our observed gravity and Moho trends have important implications for models of basin and ring formation. They suggest that impact-basin formation causes deep-seated crustal and mantle deformation on the Moon, similar to, but greater in magnitude, than the modeled mantle deformation at the Chicxulub structure on Earth. There appears to be a link between substantial crustal and mantle uplifts and peak-ring formation, which supports models involving the interaction of the huge vertical uplift confined to the center of the basin and the inward-collapsing transient cavity during the modification stage of the impact event. These results may be further extended to understanding multi-ring basin formation, particularly if peak-ring basins and the crustal deformation that characterize them are precursors to these larger impact structures.

Acknowledgements

We thank the GRAIL science team and JPL for their efforts in obtaining and processing the data that went into this work. Detailed reviews by Mark Cintala and an anonymous reviewer helped to improve the quality of the manuscript. We greatly acknowledge support from NASA as a GRAIL participating scientist (grant NNX09AI46G, to JWH) and as a GRAIL Co-Investigator (MIT subcontract to RJP).

Appendix A. Mare contribution to gravity within peak-ring basins

There are six peak-ring basins analyzed here that contain mare deposits (Table 1). The spatial extents and thicknesses of those lava deposits within these basins are variable, but in no case was the mare thick enough to cover the peak rings, implying mare thicknesses <2 km based on recent height measurements of lunar peak rings (Baker et al., 2012). Mare patches in Schrödinger are very localized and small in areal extent and are therefore inferred to be thin (<∼100 m) with a negligible contribution to the central gravity anomaly. Floor units interior to the peak ring of Lorentz have been obscured by ejecta from the complex craters Nernst and Röntgen, so it is unclear how much mare is present there.

We attempted to estimate the mare thickness interior to the peak ring in each of the remaining four peak-ring basins (Poincaré, Schiller-Zucchius, Grimaldi, and Apollo) through comparisons with recent morphometric measurements. Williams and Zuber (1998) used their measured depth-diameter trends for those structures without identifiable mare to estimate the thicknesses of lava in those basins with interior deposits. This method assumed that the relatively smaller depths of mare-filled basins were completely the result of the added thickness of the mare. However, most of the basins with mare fill are much more degraded and have wall heights reduced by as much as 2 km compared to those used for depth-diameter measurements. Therefore, mare thicknesses determined with the methods of Williams and Zuber (1998) are likely to be overestimates. If we first adjust the wall

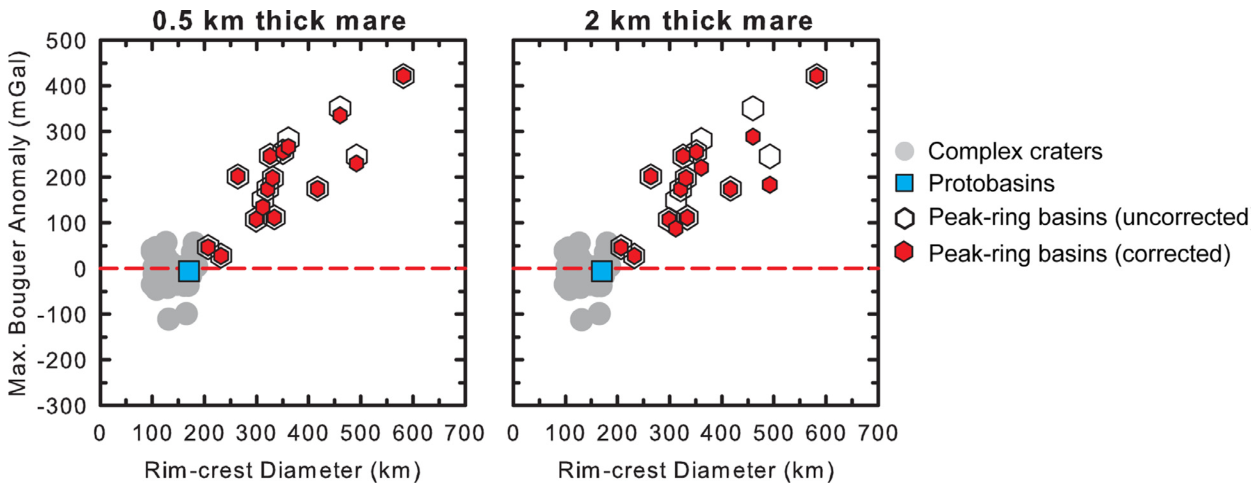

Fig. A1. Maximum Bouguer gravity anomaly (BA) within 0.5*R* as a function of rim-crest diameter for complex craters (gray circles), protobasins (blue squares), and peak-ring basins (open black hexagons and solid red hexagons). The maximum BA for peak-ring basins prior to correcting for the gravity contributions from mare are given as open black hexagons. Corrections for a 0.5 km (left panel) and 2 km (right panel) thick mare deposit within peak-ring basins are shown as solid red hexagons. With the exception of four basins (Poincaré, Schiller-Zucchius, Grimaldi, and Apollo), most peak-ring basins did not require corrections due to the absence of mare or undetermined mare extents. All complex craters and protobasins with mare deposits were excluded from the plots, as corrections were not attempted for their more complex geometries and inferred thinner deposits. See Appendix A for a description of the corrections. (For interpretation of the references to colour in this figure legend, the reader is referred to the web version of this article.)

heights to the trend of wall heights for the best preserved structures (Baker et al., 2012) and use the method of Williams and Zuber (1998) with depth trends determined by Baker et al. (2012), we calculate a wide range of mare thicknesses from ~0.5 km to 2 km for Poincaré, Schiller-Zucchius, Grimaldi, and Apollo. This range includes measurement uncertainties in depth and wall heights (where wall height is defined as the difference in elevation between the rim crest and the base of the wall; see Baker et al., 2012). Unfortunately, the number of superposed impact craters and the highly variable nature of the rim-crest elevations used to determine the depths of degraded basins precludes us from making more confident predictions of mare thicknesses from morphometric measurements alone.

Using an approximate range of 0.5 to 2 km for the mare thicknesses, we can calculate a range of plausible values for the maximum vertical gravity component contributed by the mare infill. We approximate the shape of the mare fill by a vertical cylinder with a radius R_{cyl} and thickness, t_{cyl}; the radius is estimated by fitting a circle to the mare's radial extent using LROC visual images. The geometries of the mare deposits are unlikely to be cylinders; rather, the deposits probably thin with radial distance from the basin center. Therefore, our simple approximation will produce slight overestimates of the vertical gravitational attraction of the mare infill compared with those of more realistic geometries. The vertical gravitational acceleration resulting from a cylinder (g_{cyl}) at the surface is determined using the following equation (Telford et al., 1990, their Eq. (2.59)):

$$g_{cyl} = 2\pi G\Delta\rho\left[t_{cyl} + R_{cyl} - \left({R_{cyl}}^2 + {t_{cyl}}^2\right)^{0.5}\right]$$

where G is the universal gravitational constant ($6.6738 \times 10^{-11}\ \mathrm{m^3\,kg^{-1}\,s^{-2}}$) and $\Delta\rho$ is the density contrast between the mare and surrounding rock. Note that this equation calculates g_{cyl} along the central axis and at the surface, which gives a maximum value (Telford et al., 1990, p. 38). We assume a mare density of $3300\ \mathrm{kg\,m^{-3}}$ (Wieczorek et al., 2006) and highlands density of $2550\ \mathrm{kg\,m^{-3}}$ (Wieczorek et al., 2013), resulting in $\Delta\rho = 750\ \mathrm{kg\,m^{-3}}$. Due to the mare deposits being much larger in radial extent than their thicknesses ($R >> t_{cyl}$), the calculated gravity is mostly dependent on the assumed thickness and is nearly equal to the gravitational attraction of an infinite slab ($2\pi G\Delta\rho t_{cyl}$). Using this equation, a mare thickness of 0.5 km yields an estimated gravity anomaly of 16 mGal for each of the basins, with a 2-km thick mare deposit yielding values of 62 mGal. Thus, two kilometers of basalt can have an appreciable effect on the measured maximum central gravity anomalies of these basins. Such a deposit is likely to be an upper limit, since in basins whose peak rings are still visible, any basalts would have to be less than 2-km thick because peak rings are generally less than 2 km high (Baker et al., 2012). Further, g_{cyl} may be smaller if a reduced density contrast $\Delta\rho$ is assumed, and if modeled at spacecraft altitude above the surface of the mare. However, as previous workers concluded for the more extensively infilled multi-ring basins (e.g., Phillips and Dvorak, 1981; Neumann et al., 1996), the mare cannot account for the entire observed central Bouguer anomaly signal in peak-ring basins. As described, the observed maximum BAs for Poincaré, Schiller-Zucchius, Grimaldi, and Apollo are much larger, ranging from 150 mGal to 350 mGal. Mare fill within complex craters is likely to be thinner than in peak-ring basins due to relatively less impact melt produced and retained at these sizes (Cintala and Grieve, 1998a,b) and may be contributing to some of the positive BAs observed over the locations of the floor surrounding central peaks. However, estimating the gravity contribution of mare within complex craters requires a more advanced model due to the irregular spatial and subsurface geometries of the deposits. We do not attempt to model these here, but this should be a focus for more detailed investigations. All complex craters with mare fill are noted in Table 1.

Fig. A1 shows how corrections for a 0.5 km or 2 km thick cylindrical mare deposit within Poincaré, Schiller-Zucchius, Grimaldi, and Apollo would affect the trends in maximum central Bouguer gravity anomalies with rim-crest diameter. For comparison, Fig. A1 also includes those peak-ring basins without mare and have therefore not been corrected. In these plots, we removed those complex craters and protobasins with mare infill. As shown, accounting for the effects of mare in craters and peak-ring basins does not substantially alter the trends in central maximum BAs. This provides confidence in our interpretations of the GRAIL gravity trends prior to corrections for mare infill. Due to the large uncertainties in mare thickness estimates and the relatively small influence on the overall trends in gravity, we choose to report only uncorrected values. More detailed analyses of the basin gravity signal will require improved estimates of mare thickness, likely provided by a combination of morphometric measurements and geophysical modeling.

Supplementary materials

Supplementary material associated with this article can be found, in the online version, at doi:10.1016/j.icarus.2017.03.024.

References

Abramov, O., Wong, S.M., Kring, D.A., 2012. Differential melt scaling for oblique impacts on terrestrial planets. Icarus 218, 906–916. doi:10.1016/j.icarus.2011.12.022.

Alexopoulos, J.S., McKinnon, W.B., 1994. Large impact craters and basins on Venus, with implications for ring mechanics on the terrestrial planets. In: Dressler, B.O., Grieve, R.A.F., Sharpton, V.L. (Eds.), Large Meteorite Impacts and Planetary Evolution. Special Paper 293, Geological Society of America, Boulder, CO, pp. 29–50.

Andrews-Hanna, J.C., 2013. The origin of the non-mare mascon gravity anomalies in lunar basins. Icarus 222, 159–168. doi:10.1016/j.icarus.2012.10.031.

Baker, D.M.H., Head, J.W., 2013. New morphometric measurements of craters and basins on Mercury and the Moon from MESSENGER and LRO altimetry and image data: An observational framework for evaluating models of peak-ring basin formation. Planet. Space Sci. 86, 91–116. doi:10.1016/j.pss.2013.07.003.

Baker, D.M.H., Head, J.W., Fassett, C.I., Kadish, S.J., Smith, D.E., Zuber, M.T., Neumann, G.A., 2011a. The transition from complex crater to peak-ring basin on the Moon: New observations from the Lunar Orbiter Laser Altimeter (LOLA) instrument. Icarus 214, 377–393. doi:10.1016/j.icarus.2011.05.030.

Baker, D.M.H., Head, J.W., Schon, S.C., Ernst, C.M., Prockter, L.M., Murchie, S.L., Denevi, B.W., Solomon, S.C., Strom, R.G., 2011b. The transition from complex crater to peak-ring basin on Mercury: New observations from MESSENGER flyby data and constraints on basin formation models. Planet. Space Sci. 59, 1932–1948. doi:10.1016/j.pss.2011.05.010.

Baker, D.M.H., Head, J.W., Neumann, G.A., Smith, D.E., Zuber, M.T., 2012. The transition from complex craters to multi-ring basins on the Moon: Quantitative geometric properties from Lunar Reconnaissance Orbiter Lunar Orbiter Laser Altimeter (LOLA) data. J. Geophys. Res. 117 (E00H16). doi:10.1029/2011JE004021.

Baker, D.M.H., Head, J.W., Collins, G.S., Potter, R.W.K., 2016. The formation of peak-ring basins: Working hypotheses and path forward in using observations to constrain models of impact-basin formation. Icarus 273, 146–163. doi:10.1016/j.icarus.2015.11.033.

Baldwin, R.B., 1949. The Face of the Moon. University Chicago Press, Chicago, IL, p. 239.

Barr, A.C., Citron, R.I., 2011. Scaling of melt production in hypervelocity impacts from high-resolution numerical simulations. Icarus 211, 913–916. doi:10.1016/j.icarus.2010.10.022.

Bierson, C.J., Phillips, R.J., Nimmo, F., Besserer, J., Milbury, C., Keane, J.T., Soderblom, J.M., Zuber, M.T., 2016. Interactions between complex craters and the lunar crust: Analysis using GRAIL data. J. Geophys. Res. 121, 1488–1497, doi:10.1002/2016JE005090.

Bray, V.J., Atwood-Stone, C., McEwen, A.M., 2012. Investigating the transition from central peak to peak-ring basins using central feature volume measurements from the global lunar DTM 100 m. Geophys. Res. Lett. 39 (L21201). doi:10.1029/2012GL053693.

Christeson, G.L., Collins, G.S., Morgan, J.V., Gulick, S.P.S., Barton, P.J., Warner, M.R., 2009. Mantle deformation beneath the Chicxulub impact crater. Earth Planet. Sci. Lett. 284, 249–257. doi:10.1016/j.epsl.2009.04.033.

Cintala, M.J., Grieve, R.A.F., 1998a. Scaling impact melting and crater dimensions: Implications for the lunar cratering record. Meteorit. Planet. Sci. 33, 889–912. doi:10.1111/j.1945-5100.1998.tb01695.x.

Cintala, M.J., Grieve, R.A.F., 1998b. Erratum: Scaling impact melting and crater dimensions: Implications for the lunar cratering record. Meteorit. Planet. Sci. 33, 1343. doi:10.1111/j.1945-5100.1998.tb01320.x.

Collins, G.S., Melosh, H.J., Morgan, J.V., Warner, M.R., 2002. Hydrocode simulations of Chicxulub crater collapse and peak-ring formation. Icarus 157, 24–33. doi:10.1006/icar.2002.6822.

Dence, M.R., 1973. Dimensional analysis of impact structures. Meteoritics 8, 343–344.

Dombard, A.J., Hauck, S.A., Balcerski, J.A., 2013. On the origin of mascon basins on the Moon (and beyond). Geophys. Res. Lett. 40, 28–32. doi:10.1029/2013GL054310.

Freed, A.M., Johnson, B.C., Blair, D.M., Melosh, H.J., Neumann, G.A., Phillips, R.J., Solomon, S.C., Wieczorek, M.A., Zuber, M.T, 2014. The formation of lunar mascon basins from impact to contemporary form. J. Geophys. Res. 119. doi:10.1002/2014JE004657.

Frey, H., 2011. Previously unknown large impact basins on the Moon: implications for lunar stratigraphy. In: Ambrose, W.A., Williams, D.A. (Eds.), Recent Advances and Current Research Issues in Lunar Stratigraphy. Special Paper 477, Geological Society of America, Boulder, CO, pp. 53–75.

Hale, W., Head, J.W., 1979. Central peaks in lunar craters: Morphology and morphometry. In: Proceedings of Lunar and Planetary Science Conference 10th, pp. 2623–2633.

Hartmann, W.K., Kuiper, G.P., 1962. Concentric structures surrounding lunar basins. Commun. Lunar and Planet. Lab., Univ. Arizona 1, 51–66.

Hartmann, W.K., Wood, C.A., 1971. Moon: origin and evolution of multi-ring basins. Moon 3, 3–78. doi:10.1007/BF00620390.

Head, J.W., 1974. Orientale multi-ringed basin interior and implications for the petrogenesis of lunar highland samples. Moon 11, 327–356. doi:10.1007/BF00589168.

Head, J.W., 1977. Origin of outer rings in lunar multi-ringed basins: evidence from morphology and ring spacing. In: Roddy, D.J., Pepin, R.O., Merrill, R.B. (Eds.), Impact and Explosion Cratering. Pergamon Press, New York, pp. 563–573.

Head, J.W., 2010. Transition from complex craters to multi-ringed basins on terrestrial planetary bodies: Scale-dependent role of the expanding melt cavity and progressive interaction with the displaced zone. Geophys. Res. Lett. 37 (L02203). doi:10.1029/2009GL041790.

Head, J.W., Fassett, C.I., Kadish, S.J., Smith, D.E., Zuber, M.T., Neumann, G.A., Mazarico, E., 2010. Global distribution of large lunar craters: implications for resurfacing and impactor populations. Science 329, 1504–1507. doi:10.1126/science.1195050.

Holsapple, K.A., 1993. The scaling of impact processes in planetary sciences. Annu. Rev. Earth Planet. Sci. 21, 333–373. doi:10.1146/annurev.ea.21.050193.002001.

Ishihara, Y., Morota, T., Nakamura, R., Goossens, S., Sasaki, S., 2011. Anomalous Moscoviense basin: single oblique impact or double impact origin? Geophys. Res. Lett. 38 (L03201). doi:10.1029/2010GL045887.

Ivanov, B., 2005. Numerical modeling of the largest terrestrial meteorite craters. Solar Sys. Res. 39, 381–409. doi:10.1007/s11208-005-0051-0.

Johnson, B.C., Blair, D.M., Collins, G.S., Melosh, H.J., Freed, A.M., Taylor, G.J., Head, J.W., Wieczorek, M.A., Andrews-Hanna, J.C., Nimmo, F., Keane, J.T., Miljković, K., Soderblom, J.M., Zuber, M.T., 2016. Formation of the Orientale lunar multiring basin. Science 354, 441–444. doi:10.1126/science.aag0518.

Jozwiak, L.M., Head, J.W., Zuber, M.T., Smith, D.E., Neumann, G.A., 2012. Lunar floor-fractured craters: Classification, distribution, origin and implications for magmatism and shallow crustal structure. J. Geophys. Res. 117 (E11005). doi:10.1029/2012JE004134.

Kenkmann, T., Collins, G.S., Wünnemann, K., 2013. The modification stage of crater formation. In: Osinski, G.R., Pierazzo, E. (Eds.), Impact Cratering: Processes and Products. Wiley-Blackwell, Hoboken, NJ, pp. 60–75.

Konopliv, A.S., Park, R.S., Yuan, D.-N., Asmar, S.W., Watkins, M.M., Williams, J.G., Fahnestock, E., Kruizinga, G., Paik, M., Strekalov, D., Harvey, N., Smith, D.E., Zuber, M.T., 2013. The JPL lunar gravity field to spherical harmonic degree 660 from the GRAIL primary mission. J. Geophys. Res. 118, 1415–1434. doi:10.1002/jgre.20097.

Lemoine, F.G., Goossens, S., Sabaka, T.J., Nicholas, J.B., Mazarico, E., Rowlands, D.D., Loomis, B.D., Chinn, D.S., Neumann, G.A., Smith, D.E., Zuber, M.T., 2014. GRGM900C: a degree 900 lunar gravity model from GRAIL primary and extended mission data. Geophys. Res. Lett. 41, 3382–3389. doi:10.1002/2014GL060027.

Losiak, A., Wilhelms, D.E., Byrne, C.J., Thaisen, K., Weider, S.Z., Kohout, T., O'Sullivan, K., Kring, D.A., 2009. A new lunar impact crater database. Lunar Planet. Sci. 40 no. 1532.

Melosh, H.J., 1989. Impact Cratering: A Geologic Process. Oxford University Press, London, p. 253 pp.

Melosh, H.J., Freed, A.M., Johnson, B.C., Blair, D.M., Andrews-Hanna, J.C., Neumann, G.A., Phillips, R.J., Smith, D.E., Solomon, S.C., Wieczorek, M.A., Zuber, M.T., 2013. The origin of lunar mascon basins. Science 340, 1552–1555. doi:10.1126/science.1235768.

Morgan, J., Warner, M., Grieve, R.A.F., 2002. Geophysical constraints on the size and structure on the Chicxulub impact crater. In: Köberl, C., MacLeod, K.G. (Eds.), Catastrophic Events and Mass Extinctions: Impacts and Beyond. Special Paper 356, Geological Society of America, Boulder, CO, pp. 39–46.

Morgan, J.V., Warner, M.R., Collins, G.S., Grieve, R.A.F., Christeson, G.L., Gulick, S.P.S., Barton, P.J., 2011. Full waveform tomographic images of the peak ring at the Chicxulub impact crater.. J. Geophys. Res. 116 (B06303) (B06303). doi:10.1029/2010JB008015.

Muller, P.M., Sjogren, W.L., 1968. Mascons: Lunar mass concentrations. Science 161, 680–684. doi:10.1126/science.161.3842.680.

Nahm, A.L., Öhman, T., Kring, D.A., 2013. Normal faulting origin for the Cordillera and Outer Rook Rings of Orientale basin, the Moon. J. Geophys. Res. 118, 1–16. doi:10.1002/jgre.20045.

Namiki, N., Iwata, T., Matsumoto, K., Hanada, H., Noda, H., Goossens, S., Ogawa, M., Kawano, N., Asari, K., Tsuruta, S., Ishihara, Y., Liu, Q., Kikuchi, F., Ishikawa, T., Sasaki, S., Aoshima, C., Kurosawa, K., Sugita, S., Takano, T., 2009. Farside gravity field of the Moon from four-way Doppler measurements of SELENE (Kaguya). Science 323, 900–905. doi:10.1126/science.1168029.

Neumann, G.A., Zuber, M.T., Smith, D.E., Lemoine, F.G., 1996. The lunar crust: Global structure and signature of major basins. J. Geophys. Res. 101 (E7), 16841–16843. doi:10.1029/96JE01246.

Neumann, G.A., Zuber, M.T., Wieczorek, M.A., Head, J.W., Baker, D.M.H., Solomon, S.C., Smith, D.E., Lemoine, F.G., Mazarico, E., Sabaka, T.J., Goossens, S.J., Melosh, H.J., Phillips, R.J., Asmar, S.W., Konopliv, A.S., Williams, J.G., Sori, M.M., Soderblom, J.M., Miljković, K., Andrews-Hanna, J.C., Nimmo, F., Kiefer, W.S., 2015. Lunar impact basins revealed by Gravity Recovery and Interior Laboratory measurements. Sci. Adv. 1. doi:10.1126/sciadv.1500852.

Osinski, G.R., Tornabene, L.L., Grieve, R.A.F., 2011. Impact ejecta emplacement on terrestrial planets. Earth Planet. Sci. Lett. 310, 167–181. doi:10.1016/j.epsl.2011.08.012.

Phillips, R.J., Dvorak, J., 1981. The origin of lunar mascons: Analysis of the Bouguer gravity associated with Grimaldi. In: Schultz, P.H., Merrill, R.B. (Eds.), Multi-Ring Basins: Formation and Evolution. Proceedings of Lunar and Planetary Science, 12A, pp. 91–104.
Pierazzo, E., Melosh, H.J., 2000. Understanding oblique impacts from experiments, observations, and modeling. Ann. Rev. Earth Planet. Sci. 28, 141–167. doi:10.1146/annurev.earth.28.1.141.
Pierazzo, E., Vickery, A.M., Melosh, H.J., 1997. A reevaluation of impact melt production. Icarus 127, 408–423. doi:10.1006/icar.1997.5713.
Pike, R.J., 1982. Crater peaks to basin rings: The transition on Mercury and other bodies. NASA Tech. Memo. TM-85127 117–119.
Pike, R.J., 1988. In: Vilas, F., Chapman, C.R., Matthews, M.S. (Eds.), Geomorphology of Impact Craters on Mercury. Mercury. University Arizona Press, Tucson, AZ, pp. 165–273.
Pike, R.J., Spudis, P.D., 1987. Basin-ring spacing on the Moon, Mercury, and Mars. Earth Moon Planets 39, 129–194. doi:10.1007/BF00054060.
Potter, R.W.K., 2015. Investigating the onset of multi-ring impact basin formation. Icarus 261, 91–99. doi:10.1016/j.icarus.2015.08.009.
Potter, R.W.K., Kring, D.A., Collins, G.S., Kiefer, W.S., McGovern, P.J., 2012. Estimating transient crater size using the crustal annular bulge: Insights from numerical modeling of lunar basin-scale impacts. Geophys. Res. Lett. 39 (L18203). doi:10.1029/2012GL052981.
Potter, R.W.K., Kring, D.A., Collins, G.S., Kiefer, W.S., McGovern, P.J., 2013. Numerical modeling of the formation and structure of the Orientale impact basin. J. Geophys. Res. 118, 963–979. doi:10.1002/jgre.20080.
Schultz, P.H., 1976. Floor-fractured lunar craters. Moon 15, 241–273.
Soderblom, J.M., Evans, A.J., Johnson, B.C., Melosh, H.J., Miljković, K., Phillips, R.J., Andrews-Hanna, J.C., Bierson, C.J., Head, J.W., Milbury, C., Neumann, G.A., Nimmo, F., Smith, D.E., Solomon, S.C., Sori, M.M., Wieczorek, M.A., Zuber, M.T., 2015. The fractured Moon: production and saturation of porosity in the lunar highlands from impact cratering. Geophys. Res. Lett. **42**. 6939–6944, doi:10.1002/2015GL065022.
Spudis, P.D., 1993. The Geology of Multi-Ring Impact Basins 177.
Telford, W.M., Geldart, L.P., Sheriff, R.E., 1990. Applied Geophysics. Cambridge Univ. Press, New York, p. 770 pp..
Thaisen, K.G., Head, J.W., Taylor, L.A., Kramer, G.Y., Isaacson, P., Nettles, J., Petro, N., Pieters, C.M., 2011. Geology of Moscoviense basin. J. Geophys. Res. 116. (E00G07), doi:10.1029/2010JE003732.
Turtle, E.P., Pierazzo, E., Collins, G.S., Osinski, G.R., Melosh, H.J., Morgan, J.V., Reimold, W.U., 2005. Impact structures: What does crater diameter mean?. In: Kenkmann, T., Hörz, F., Deutsch, A. (Eds.) Large Meteorite Impacts and Planetary Evolution III. Special Paper 384, Geological Society of America, Boulder, CO, pp. 1–24.
Vaughan, W.M., Head, J.W., Wilson, L., Hess, P.C., 2013. Geology and petrology of enormous volumes of impact melt on the Moon: A case study of the Orientale basin impact melt sea. Icarus 223, 749–765. doi:10.1016/j.icarus.2013.01.017.
Wieczorek, M.A., Phillips, R.J., 1998. Potential anomalies on a sphere: Applications to the thickness of the lunar crust. J. Geophys. Res. 103, 1715–1724. doi:10.1029/97JE03136.
Wieczorek, M.A., Phillips, R.J., 1999. Lunar multiring basins and the cratering process. Icarus 139, 246–259. doi:10.1006/icar.1999.6102.
Wieczorek, M.A., Jolliff, B.L., Khan, A., Pritchard, M.E., Weiss, B.P., Williams, J.G., Hood, L.L., Righter, K., Neal, C.R., Shearer, C.K., McCallum, I.S., Tompkins, S., Hawke, B.R., Peterson, C., Gillis, J.J., Bussey, B., 2006. The constitution and structure of the lunar interior. Rev. Min. Geochem 60, 221–364. doi:10.2138/rmg.2006.60.3.
Wieczorek, M.A., Neumann, G.A., Nimmo, F., Kiefer, W.S., Taylor, G.J., Melosh, H.J., Phillips, R.J., Solomon, S.C., Andrews-Hanna, J.C., Asmar, S.W., Konopliv, A.S., Lemoine, F.G., Smith, D.E., Watkins, M.M., Williams, J.G., Zuber, M.T., 2013. The crust of the Moon as seen by GRAIL. Science 339, 671–675. doi:10.1126/science.1231530.
Wilhelms, D.E., 1987. The geologic history of the Moon. USGS Prof. Paper 1348, 302 pp.
Williams, K.K., Zuber, M.T., 1998. Measurement and analysis of lunar basin depths from Clementine altimetry. Icarus 131, 107–122. doi:10.1006/icar.1997.5856.
Wise, D.U., Yates, M.T., 1970. Mascons as structural relief on a lunar "Moho. J. Geophys. Res. 75, 261–268. doi:10.1029/JB075i002p00261.
Wood, C.A, Head, J.W., 1976. Comparisons of impact basins on Mercury, Mars and the Moon. In: Proceedings of Lunar and Planetary Science Conference 7th, pp. 3629–3651.
Wünnemann, K., Morgan, J.V., Jödicke, H., 2005. Is Ries crater typical for its size? An analysis based upon old and new geophysical data and numerical modeling. In: Kenkmann, T., Hörz, F., Deutsch, A. (Eds.), Large Meteorite Impacts III. Special Paper 384, Geological Society of America, Boulder, CO, pp. 67–83.
Zuber, M.T., Smith, D.E., Lehman, D.H., Hoffman, T.L., Asmar, S.W., Watkins, M.M., 2013a. Gravity Recovery and Interior Laboratory (GRAIL): Mapping the lunar interior from crust to core. Space Sci. Rev. 178, 3–24. doi:10.1007/s11214-012-9952-7.
Zuber, M.T., Smith, D.E., Watkins, M.M., Asmar, S.W., Konopliv, A.S., Lemoine, F.G., Melosh, H.J., Neumann, G.A., Phillips, R.J., Solomon, S.C., Wieczorek, M.A., Williams, J.G., Goossens, S.J., Kruizinga, G., Mazarico, E., Park, R.S., Yuan, D.-N., 2013b. Gravity field of the Moon from the Gravity Recovery and Interior Laboratory (GRAIL) mission. Science 339, 668–671. doi:10.1126/science.1231507.
Zuber, M.T., Smith, D.E., Neumann, G.A., Goossens, S., Andrews-Hanna, J.C., Head, J.W., Kiefer, W.S., Asmar, S.W., Konopliv, A.S., Lemoine, F.G., Matsuyama, I., Melosh, H.J., McGovern, P.J., Nimmo, F., Phillips, R.J., Solomon, S.C., Taylor, G.J., Watkins, M.M., Wieczorek, M.A., Williams, J.G., Jansen, J.C., Johnson, B.C., Keane, J.T., Mazarico, E., Miljković, K., Park, R.S., Soderblom, J.M., Yuan, D.-N., 2016. Gravity field of the Orientale basin from the Gravity Recovery and Interior Laboratory mission. Science 354, 438–441. doi:10.1126/science.aag0519.